Cement and Concrete Research 54 (2013) 161–179

Contents lists available at ScienceDirect

Cement and Concrete Research

journal homepage: http://ees.elsevier.com/CEMCON/default.asp

# Photovoltaic's silica-rich waste sludge as supplementary cementitious material (SCM)

G. Quercia [a,b,*], J.J.G. van der Putten [b], G. Hüsken [c], H.J.H. Brouwers [b]

[a] Materials innovation institute (M2i), Mekelweg 2, P.O. Box 5008, 2600 GA Delft, The Netherlands
[b] Eindhoven University of Technology, Department of the Built Environment, P.O. Box 513, 5600 MB Eindhoven, The Netherlands
[c] BAM Federal Institute for Materials Research and Testing, Unter den Eichen 87, D-12205 Berlin, Germany

ARTICLE INFO

*Article history:*
Received 18 December 2012
Accepted 15 August 2013
Available online xxxx

*Keywords:*
Nano-silica sludge (D)
Supplementary cementitious materials (D)
Pozzolanic index (C)
Mortar (E)

ABSTRACT

Waste sludge, a solid recovered from wastewater of photovoltaic-industries, composes of agglomerates of nano-particles like $SiO_2$ and $CaCO_3$. This sludge deflocculates in aqueous solutions into nano-particles smaller than 1 μm. Thus, this sludge constitutes a potentially hazardous waste when it is improperly disposed. Due to its high content of amorphous $SiO_2$, this sludge has a potential use as supplementary cementitious material (SCM) in concrete. In this study the main properties of three different samples of photovoltaic's silica-rich waste sludge (nSS) were physically and chemically characterized. The characterization techniques included: scanning electron microscopy (SEM), X-ray energy dispersive spectroscopy (EDS), X-ray diffraction (XRD), nitrogen physical adsorption isotherm (BET method), density by Helium pycnometry, particle size distribution determined by laser light scattering (LLS) and zeta-potential measurements by dynamic light scattering (DLS). In addition, a dispersability study was performed to design stable slurries to be used as liquid additives for the concrete production on site. The effects on the hydration kinetics of cement pastes by the incorporation of nSS in the designed slurries were determined using an isothermal calorimeter. A compressive strength test of standard mortars with 7% of cement replacement was performed to determine the pozzolanic activity of the waste nano-silica sludge. Finally, the hardened system was fully characterized to determine the phase composition. The results demonstrate that the nSS can be utilized as SCM to replace portion of cement in mortars, thereby decreasing the $CO_2$ footprint and the environmental impact of concrete.



## 1. Introduction

Photovoltaic or PV is the technology which converts sunlight into electricity. With increasing concerns surrounding the global climate and the uncertainty of oil sources and prices among other traditional fuels, the solar power industry has been growing substantially in recent years. Since 1990, photovoltaic module installed power had increased more than 500 times from 46 megawatts (MW) to 30.8 GW in 2012 [1], making it the world's fastest-growing energy technology. Due to the rapid expansion of the silicon Photovoltaic industry it receives increased attention because of the potential environmental impact of their process and products. Decommissioning at the end of the life cycle of PV modules, which are expected to last around 30 years [2], is an important factor. There are also concerns regarding their disposal as they may contain small amounts of regulated materials. Different researchers have focused on the recycling waste streams from the PV slicing production process. Wang et al. [3] published a novel approach for recycling "kerf" loss from the cutting slurry waste. Also Kong et. al. [4] made efforts to recycle silicon powder from the silicon wafer back grinding. Recently, researchers [3,5] suggest the use of cement based material fixation capacity to the possible re-utilization of solar cell residue to construction materials, which will lower the costs and help to decrease the waste disposal from PV systems.

Nowadays supplementary cementitious materials (SCMs) are widely used in concrete either in blended cements or added separately to the concrete mix [6]. The use of silica-rich SCM such as blast furnace slag, fly ash, metakaolin and micro-silica represents a viable solution to partially replace ordinary Portland cement. Other possible materials, which are under research worldwide, are silica fines. They are mainly composed of high purity $SiO_2$ with micron and submicron particles. Examples of this are silica flour (Sf), micro-silica (mS), fumed silica (FS) and nano-silica (nS). However, these products are obtained in complex processes which make their use non-feasible due to their price or in some case their availability for the construction industry [7,8]. In this context, another potential source of nano-silica particles is the waste sludge, generated during the polishing process of photovoltaic (PV) solar panels [9]. This waste sludge is collected during the filtering steps of the slurry used in the polishing or finishing process of the silicon solar panels by chemical mechanical planarization (CMP) [10]. In South Korea, 50,000 tons of CMP silica sludge are generated annually. The

* Corresponding author at: Materials innovation institute (M2i), Mekelweg 2, P.O. Box 5008, 2600 GA Delft, The Netherlands.
*E-mail address:* g.quercia@tue.nl (G. Quercia).

0008-8846/$ – see front matter © 2013 Elsevier Ltd. All rights reserved.
http://dx.doi.org/10.1016/j.cemconres.2013.08.010

polishing slurries are usually composed of a stable colloidal nano-silica, fumed silica, nano-$CaCO_3$ and other types of suspensions [9–12]. This sludge deflocculates in aqueous solutions into nano-particles smaller than 1 μm. Thus, this nano-silica sludge (nSS) is potentially hazardous waste when it is improperly dumped. The feasibility to use waste sludge from semiconductor industry in cement mortars was established for the first time by Lee and Liu in 2009 [13] and later by other researchers [14–16]. However, the use of waste sludge from PV panel CMP process has not been studied yet.

In addition to the need to improve the properties of concrete, the environmental impact of the cement used in concrete industry is becoming an important issue. The component with the highest environmental impact that is used for concrete production in terms of energy and $CO_2$ emissions is cement clinker. In general, 0.85 ton of $CO_2$ is released when 1 ton of cement clinker is produced [17]. It is calculated that cement clinker production contributes 5 to 8% to the total $CO_2$ emissions worldwide [17]. Consequently, the construction sector demands concrete with a lower environmental impact. Based on these premises, the aim of this research is to determine the potential use of photovoltaic's silica-rich sludge as supplementary cementitious material (SCM) in concrete. In this study, the main properties of three different samples of photovoltaic's silica-rich waste sludge were physically and chemically characterized. The final goal is to demonstrate that the nSS can be utilized as SCM to replace portion of cement in mortars, thereby decreasing the $CO_2$ footprint of concrete and to avoid the environmental impact of PV waste landfill.

In this research, the initial characterization and testing of different silica-rich waste sludges (nSS) obtained from one South Korean photovoltaic panel producer are presented. To access the potential use of nSS as supplementary cementitious material, three different batches of nSS were physically and chemically characterized. In addition, a dispersability study was performed to design stable slurries to be used as liquid additives for the concrete production on site. The designed slurries were tested using an isothermal calorimeter. Finally, standard cement pastes and mortars with 7% by weight of cement (bwoc) replacement were fully characterized to determine the pozzolanic activity and to assess the feasibility of the waste silica-rich sludge as supplementary cementitious material in concrete.

## 2. Materials and experimental methods

### 2.1. Materials

Three batches of CMP sludge cake from wet waste were obtained from DAE Pyung Ceramics Co., Ltd. located in South Korea. After drying at 105 °C for 24 h until a complete dry state (constant weight) was obtained, the water content of the sludge was determined to be between 33 and 39%. These cakes had ivory white color. The cement used was ordinary Type I Portland cement OPC (CEM I 52.5 N) produced by ENCI Cement, The Netherlands. The OPC had an apparent density of 3.15 g/cm$^3$ and a Blaine specific surface area of 484 m$^2$/g. The chemical composition (determined by XRF) and the proportion of mineral phases provided by the producer are shown in Table 1. Standard sand was used according to EN 196-1 [18], with particles size between 0 and 2 mm. In addition, a commercial micro-silica (mS) slurry with 50% of solid was used for comparison.

**Table 1**
Chemical analysis and phase composition of the cement used (CEM I 52.5 N).

| Oxide composition by XRF (mass %) | | Mineral composition by Rietveld refinement (mass %) [70] | |
|---|---|---|---|
| $SiO_2$ | 19.64 | Alite ($C_3S$) | 58.67 |
| $Na_2O$ | 0.35 | Belite ($C_2S$) | 17.05 |
| $Al_2O_3$ | 4.80 | Aluminate ($C_3A$) | 3.24 |
| $Fe_2O_3$ | 3.28 | Ferrite ($C_4AF$) | 10.26 |
| CaO | 63.34 | Calcite | 3.01 |
| Cl | 0.06 | Anhydrite | 2.99 |
| $P_2O_5$ | 0.59 | Bassanite | 1.16 |
| $K_2O$ | 0.06 | Syngenite | 0.94 |
| MgO | 1.99 | Ca-Langbeinite | 0.53 |
| $TiO_2$ | 0.34 | Gypsum ($C\bar{S}$) | 0.06 |
| $SO_3$ | 2.07 | Free lime (CaO) | 0.97 |
| Others | 0.62 | Periclase (MgO) | 0.97 |
| LOI | 1.56 | Others | 0.15 |

### 2.2. Experimental methods

#### 2.2.1. Particle morphological characteristics

Size and morphology of the particles of the silica sludge were analyzed using a high resolution scanning electron microscope (FEI Quanta 600 FEG-SEM) with a Schottky field emitter gun (at voltage of 10 keV and 0.6 mbar of low-vacuum pressure). Furthermore, a general chemical analysis was performed using EDAX® energy dispersive spectroscopy (EDS) detector.

#### 2.2.2. XRD and XRF of the silica sludge

Powder X-ray diffraction (XRD) analysis was carried out using an X-ray diffractometer (Rigaku, Geigerflex, Japan) with Cu $K_{\alpha 1}$ radiation and a 6 h scanning range between 5° and 100°. The XRD scans were run at 0.02° per step with a counting time of 4 s. In order to obtain a more accurate chemical composition of the investigated nano-silica sludge, a quantitative X-ray fluorescence (XRF) analysis by the fusion method (routine 4C) was performed. The results were obtained by an external laboratory (Activation Laboratories Ltd, Canada) [19]. In the XRF analysis a standard micro-silica was included as comparison.

#### 2.2.3. TG/DSC of the silica sludge

A thermal gravimetric (TG) and differential scanning calorimetric (DSC) analysis were performed to determine the amount of adsorbed water and other types of possible contaminants (carbonates, organics, etc.) in the nano-silica sludge. An STA 449 F1 Jupiter (Netzsch Instruments) was used to perform the TG/DSC analysis. The temperature was increased gradually from room temperature to 1000 °C at 10 K/min, keeping it constant for 2 h at 1000 °C. The samples were tested as received and a simple hand grinding was performed prior testing.

#### 2.2.4. Nitrogen physical adsorption isotherm (BET method)

A Micromeritics TriStar 3000 equipment using $N_2$ with a soaking time of 12 h at 120 °C was used for the gas physisorption analysis. Using the BET theory [20] and the standard procedure described by Din ISO 9277:1995 [21], the specific surface area ($SSA_{BET}$) of the silica samples was determined. The physisorption analyses were carried out three times with a standard deviation below 5% for the $SSA_{BET}$. The particle size of the nano-silica was calculated from the geometrical relationship between surface area and mass given by [22]:

$$d = \frac{6000}{\rho \cdot SSA_{BET}} \quad (1)$$

where $d$ is the particle size of nano-silica in nm, $\rho$ the density of the material in g/cm$^3$ and $SSA_{BET}$ the surface area in m$^2$/g. This particle size is an average value, considering that the particles are spherical.

#### 2.2.5. Specific density by helium pycnometry

A helium pycnometer AccuPyc® II 1340 from Micromeritics was used to determine the specific density of the different nano-silica samples. Before the density measurements, the samples were dried and degassed at 105 °C for 24 h. Helium was used as the displacement medium. Ten purges of the system were performed to ensure the equilibrium and to complete a total degassing of the sample. This was followed by 12 consecutive volume measurements, which were used to determine the average density.

*2.2.6. Particle size distribution (PSD) and zeta potential (ξ) by dynamic light scattering (DLS)*

The laser light diffraction was used to determine the particle size distribution of the original nano-silica sludge and the resulting stable slurries. The PSDs were measured in this study in liquid dispersion (water) with a Malvern™ Mastersizer™ 2000 laser light diffraction device, using Mie scattering theory as the measuring principle and following the ISO standard 13320-1 (1999) [23]. A Hydro S unit was used to disperse the samples. A spherical shape was assumed to calculate the particle size distribution.

The zeta potential of stable slurries formulated with the nano-silica sludge was measured using dynamic light scattering (Malvern™ Zetasizer™ Nano ZS) according to ISO 13321 (2006) [24]. A conventional cell was used for particle size measurement (distribution in volume) [25].

*2.2.7. Dispersability study with high shear mixer*

Due to the highly agglomerated state of the nano-silica sludge, a dispersability study was performed. For this study only a sample of nano-silica sludge (batch 2) was considered. Batch 1 was discarded for the dispersability study due to its high content of impurities (discussed in Section 3). Cakes of dried nano-silica sludge from batch 2 were pre-dispersed in water (1 wt.%) in a glass stirred vessel (1 L beaker). Dispersions were transferred to the high energy shear mixer (Silverson® L5M using a size reduction stator head). The rotor speed was set to the required value (3000 and 7000 rpm) and at each speed the dispersions were sheared for 210 min. Small samples from the dispersion were taken at certain times and the particle size distribution (PSD) was measured using LLS. In addition, zeta potential was measured to study the stability of the dispersion. A dispersion study was also performed with varying pH values of the solution prepared with 25% $NH_4OH$.

*2.2.8. Design of stable nano-silica slurries for their use as SCM*

Three different stabilized slurries were designed for their use in the calorimetry and mortar tests. Table 2 shows the different components used to obtain stable slurries. The slurries were prepared using dried silica sludge (16.5 wt.%) from different batches. Each sample was pre-dispersed for 1 h at 7000 rpm in water, using a glass stirred vessel coupled to an Ultramix® stirrer. Prior to the pre-dispersion step, $NH_4OH$ and a polycarboxylate type superplasticizer (SP) were added to stabilize the slurries and to adjust the final pH value between 9.1 and 9.6. Then the dispersions were transferred to the high shear mixer, but using a size reduction stator head for additional 30 min. The obtained slurries were stable in time. No gelling was observed over a time period of 3 weeks with static conditions.

*2.2.9. Hydration kinetics of cement pastes with nano-silica*

A calorimetric analysis of cement mortars with w/c ratio of 0.5 was performed using the slurry prepared from the nSS batch 2. For this purpose, an 8-channel TAM® Air isothermal micro calorimeter from TA Instruments (U.S.A.) was used. In total 4 different cement pastes with 0, 3, 6 and 9% of nSS based on the weight of cement (bwoc) were tested in duplicate for 72 h at 20 °C. The cement pastes were mixed with a hand mixer for 1 min. The calorimetric analysis was performed to assess whether the nano-silica sludge particles exhibit an acceleration effect or any pozzolanic activity. The results were analyzed using the TAM assistance software. By means of the software tool, the dormant period, the relative setting time and the time to reach the maximum hydration peak were determined. The dormant period, relative setting times as well as the time to reach the maximum peak were defined as proposed by [26–28]. Similarly, a second calorimetric analysis was performed using the slurries prepared from batches 1–3 and the standard micro-silica slurry. In total 4 different cement pastes with 7% by weight of cement (bwoc) replacement, w/c of 0.5 and SP content (based on the mortar recipes shown in Table 3 without sand addition) were tested in duplicate for 70 h at 20 °C. The cement pastes were mixed with a high energy (600 W) hand blender (Philips HR1363) for 2 min. The results were analyzed using the same procedure as previously described.

*2.2.10. Compressive strength of cured cement mortars and pozzolanic activity*

To determine the pozzolanic index or activity of the nSS, different cement mortars were prepared and tested following the procedure established in CEN-EN 196-1 [18]. A 7% by weight of cement replacement was selected based on the procedure described by Justnes and Ostnor [29]. In total 9 standard prisms per mix were tested following the mix designs presented in Table 3. The SP content in these mixes was adjusted to obtain a spread flow of 175 ± 15 mm (Hägermann cone). The flexural and compressive strength of the mixes was determined at 1, 7 and 28 days. Finally, the pozzolanic activity index was calculated based on the results of the standard cement mortar at 7 and 28 days. In addition, the pozzolanic index was compared with the results obtained for one commercial micro-silica slurry.

*2.2.11. Characterization of the hydrated mortars*

As the use of silica-rich waste sludge should influence the amount and kind of formed hydration phases and thus the volume, the porosity and finally the durability properties of concrete, different characterization techniques were performed to consider the photovoltaic's silica-rich sludge as supplementary cementitious material.

*2.2.11.1. Microstructural characterization and analysis.* The microstructural morphology of the prepared mortars (reference, batches 1–2 and micro-silica) was analyzed using the same ESEM/EDS devices and procedures as described in Section 2.2.1. For this analysis, 5 mm thick slides were horizontally extracted from hardened prisms at the age of 28-days using a precision diamond saw. After cutting, the samples were ground by hand and moderate pressure on the middle-speed lap wheel with p180, p320 and p600 SiC papers. Polishing was done on a lap wheel with 15, 7, 3, 1 and 0.25 μm diamond pastes for about 2 min each.

**Table 2**
Proportioning of the designed silica sludge slurries.

| Batch number | 1 | 2 | 3 |
|---|---|---|---|
| Water (g) | 600 | 600 | 600 |
| Powder nano-silica sludge (g)[a] | 200 | 200 | 200 |
| $NH_4OH$ 25% (g) | 14.3 | 14.3 | 14.3 |
| SP (PCE type) (g) | 4.4 | 4.4 | 4.4 |
| Final pH | 9.27 | 9.58 | 9.12 |
| Slurry density (g/cm$^3$) | 1.070 | 1.103 | 1.102 |
| Solid content (wt.%)[b] | 16.06 | 16.48 | 16.32 |

[a] 30 to 35% content of $H_2O$.
[b] Computed by drying 5 g of slurry at 110 °C for 24 h.

**Table 3**
Mix designs of mortars used for determining compressive strength and pozzolanic index.

| Materials | Reference | Batch 1 | Batch 2 | Batch 3 | Micro-silica |
|---|---|---|---|---|---|
| CEM I 52.5 N (g) | 450.0 | 418.5 | 418.5 | 418.5 | 418.5 |
| nSS slurry (16.5 wt.%) (g) | 0 | 196.9[a] | 196.9[a] | 196.9[a] | 0 |
| mS slurry (50 wt.%) (g) | 0 | 0 | 0 | 0 | 72.3 |
| Water (g) | 225 | 59.6 | 59.6 | 59.6 | 184.2 |
| Standard sand 0–2 mm (g) | 1350 | 1350 | 1350 | 1350 | 1350 |
| SP for standard workability (g) | 0 | 2.01 | 0.93 | 0.93 | 1.07 |
| Total SP (% bwoc) | 0 | 0.68 | 0.44 | 0.44 | 0.24 |
| w/c | 0.5 | 0.5 | 0.5 | 0.5 | 0.5 |
| Air voids (%)[b] | 6.14 | 10.98 | 6.15 | – | 3.99 |
| Slump-flow (mm), 15 strokes | 176 ± 4 | 176 ± 3 | 181 ± 4 | 180 ± 5 | 182 ± 7 |

[a] Included 0.54 wt.% of SP according to Table 2.
[b] Estimated value.

After polishing, the samples were immersed in isopropanol for three days to stop the hydration completely and then dried in an oven for extra three days at 70 °C. Finally, the samples were stored in a desiccator over silica-gel (in vacuum) until the ESEM analysis was performed. The images were obtained using the BSE detector in low vacuum mode (60 mbar) and using an acceleration voltage of 20–15 keV.

*2.2.11.2. Phase composition of the hydrated mortars by TGA/DTG and XRD.* Extracted slides of each mortar composition at the age of 28-days were soaked in isopropanol for three days to stop the hydration. Afterwards, the slides were crushed and pulverized by the use of an automatic mortar crusher for 1 min and dried at 70 °C for three days. Thermogravimetric analysis (TGA) and derivative thermogravimetric analysis (DTG) were performed using the same device as described in Section 2.2.3. A total quantity of 74–92 mg was heated at 5 K/min from 20 to 1000 °C. The tests were performed at atmospheric pressure with a nitrogen flow of 20 mL/min. Alumina ($Al_2O_3$) crucibles were used in the experiments. The amount of chemically bound water, portlandite (CH) and calcite was determined by the mass losses. The mass losses were determined in three different temperature intervals. The mass loss due to the decomposition of CH, ranging from about 410 °C to 550 °C, the mass loss corresponding to the decomposition of monocarboaluminates and calcite (release of $CO_2$), measured between 550 °C and about 750 °C, and the mass loss corresponding to the release of chemically bound water (H), defined here as the measured mass loss between 105 °C and about 1000 °C minus the mass loss due to carbonation (measured between 550 °C and about 750 °C). The start and end of each temperature interval are determined for each sample based on the DTG-curve. The mass losses were calculated taking into account the molecular weight of each component (CH, calcite and water) and were expressed as % of the dry mortar mass at 550 °C. Moreover, the mass losses of CH and calcite were corrected taking into account the original calcite content (ex. batch 2 sample) and the chemical reaction between CH an $CO_2$ (carbonation) using the methodology described in [30].

Powder X-ray diffraction (XRD) spectrums were obtained with pulverized mortar samples from the same batches used to obtain the TG/DTG profile. XRD qualitative analysis was carried out using the same device as described in Section 2.2.2 with Cu $K_{\alpha 1}$ radiation and a 2 h scanning range between 3° and 70°. The XRD scans were run at 0.05° per step with a counting time of 5 s.

*2.2.11.3. Permeable (water accessible) porosity.* To assess the permeable porosity and other related durability properties of the mortars containing nSS, two cylindrical samples (height of approximately 110 mm, diameter of 100 mm) for the reference, silica sludge batches 1–2 and for the micro-silica slurry were cast, striped after 1 day and cured under water for 28 days. Three mortar discs, two with a height of approximately 15 mm and one with a height of approximately 50 mm for each mortar mix were extracted from the inner layers of eight different cylindrical samples. In total 16 discs (15 mm in height) were used to determine the permeable porosity, following the procedure described in the ASTM 1202 [31] and the remaining discs were used for the RCM and conductivity test (Section 2.2.11.4). The vacuum-saturation technique was applied to fill the accessible pores with water, as this technique is concluded to be the most efficient by Safiuddin and Heran [32].

*2.2.11.4. Rapid Chloride Migration (RCM) test and conductivity test.* To understand the impact of cement replacement on the durability of cement pastes, the Rapid Chloride Migration test was performed. In total 8 discs (50 mm in height), two for each mix, were used for RCM tests at the age of 28 days. One day prior to the RCM test, the specimens were pre-conditioned (vacuum-saturation with limewater). The RCM test was performed according to NT Build 492 [33], using the test set-up described in [34]. The duration of the RCM test for all samples was 24 h. After the test, the penetration depth of chlorides was measured on split samples by applying a colourimetric indicator for chlorides (0.1 M $AgNO_3$ solution) and the values of the chloride migration coefficients ($D_{RCM}$) were calculated according to [33].

Before the RCM test, the electrical resistance was measured on the same saturated samples by using the so-called 'two electrodes' method [35]. For this, an AC test signal (f = 1 kHz) was applied between two stainless-steel electrodes and the resistance of the concrete sample placed between the electrodes was registered. Finally, the conductivity of the samples was calculated taking into account their thicknesses and transversal areas.

## 3. Results and discussion

### 3.1. Characterization of the PV silica-rich sludge

#### 3.1.1. FEG-SEM and EDS analysis

Fig. 1, shows the morphology of the different nSS particles of batches 1, 2 and 3 obtained using a FEG-SEM microscope. The nSS is characterized by a wide particle size distribution, containing particles in the micro- and nano-range (Fig. 1a) that show a highly agglomerated state. Angular, irregular and spherical particles are also identified. The semi-quantitative chemical analysis that was performed using an EDS detector demonstrates that the nSS batch 1 has a high content of $SiO_2$ (86–95%). Other elements that were identified were Na, Al and P. These elements probably originate from the stabilization agents that are normally used in colloidal silica products and the chemicals to treat the waste water as well. The analysis of nSS of batches 2 and 3 shows small angular and spherical particles (Fig. 1b–c). The spherical particles are composed of $SiO_2$ (silica fume), commonly used in the preparation of CMP slurries [11]. In addition, small angular particles with a high content of Ca and C (detected by EDS) were also identified. The calcium rich particles are composed of $CaCO_3$ (validated by XRD and TG/DSC analysis), which is used for CMP slurries as well [10–12]. The chemical analysis demonstrates that the silica sludge of batches 2 and 3 have a lower content of $SiO_2$ (46.8%) compared to batch 1. Other elements that were identified are C, Na, Cl, Ca, Mg, K, and Al. Another observation is that the chloride content in the samples is high, reaching values of 0.56 to 1.9%. The high chloride concentration originates, most likely, from the use of deflocculating agents of the waste treatment or from chlorates used as oxidizing agents [36]. Several authors reported [36–38] that water extracted from the sludge is normally treated with aluminum poly-chloride compounds to deflocculate the nanoparticles.

#### 3.1.2. X-ray fluorescence (XRF) and X-ray diffraction (XRD) analysis

In order to obtain detailed information on the chemical composition of the investigated nano-silica sludge, a quantitative X-ray fluorescence analysis was performed. The results are shown in Table 4. The data demonstrate that the nano-silica sludge of batch 1 is rich in $SiO_2$ (80.6%), $Al_2O_3$ (8.9%), $P_2O_5$ (3.2%) and $SO_3$ (2.1%). These results are in line with the chemical analysis performed using the EDS detector. Furthermore, it is demonstrated that the silica sludge of batches 2 and 3 is rich in CaO and $SiO_2$, with an equivalent content between 41 and 43 wt.% of $SiO_2$ and 45 to 56 wt.% of CaO. Another observation is the high concentration of chloride ($Cl^-$), confirmed in both samples (1.34 to 1.9 wt.%). This concentration of chloride is above the maximum concentration (0.3 wt.%) specified for micro-silica in NEN EN 3263-1:200 [39] and it is inclusively higher than the maximum concentration specified for Bottom ashes (0.62 wt.%) [40]. In this case, it is recommended to determine the total chloride content in these samples by titration method as it is specified in DIN EN 196-2 [41] for cement. The high chloride content would limit the application of this type of waste sludge in concrete, makes it maybe not feasible for special exposition classes.

In addition to the XRF analysis, X-ray diffraction (XRD) measurements were performed to verify whether the silica sludge has crystalline impurities. The results for the silica sludge of batch 1 are shown in

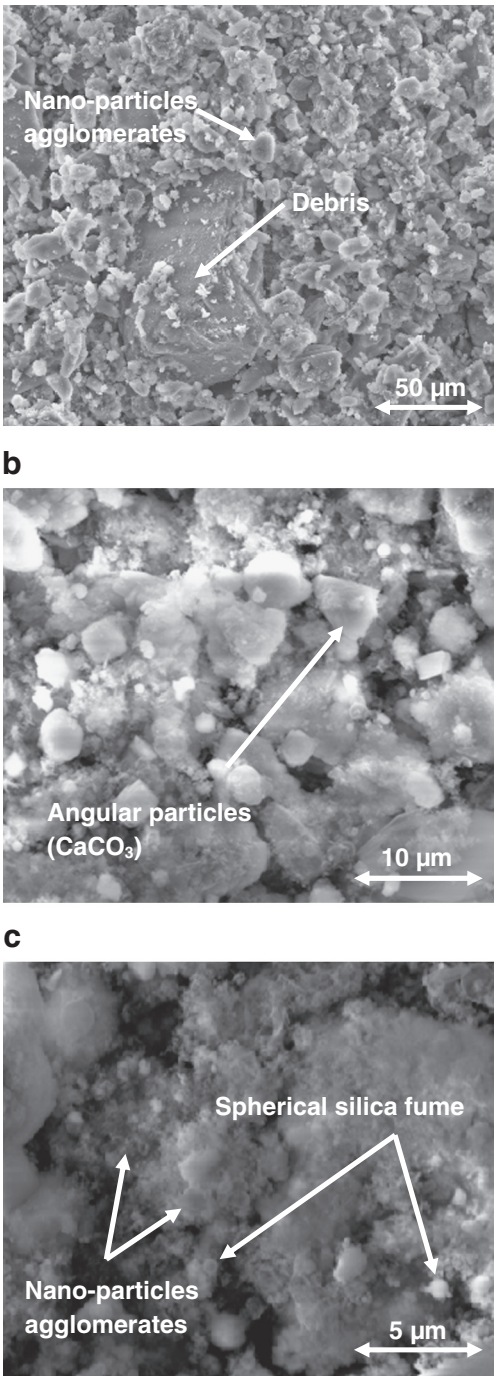


**Fig. 1.** FEG-SEM photomicrographs of nSS, a) batch 1, b) batch 2 and c) batch 3.

Fig. 2 (diffraction pattern—a). The XRD spectrum shown in Fig. 2 is typical for materials with high content of amorphous phases; no crystalline phases were identified for this batch. On the contrary, the results of the silica sludge of batches 2 and 3, shown in Fig. 2 (diffraction pattern—b and pattern—c, respectively), revealed that in these two samples the content of crystalline phases (in addition to amorphous $SiO_2$) is high. The crystalline phases identified were mainly calcium carbonates (type $CaCO_3$) and chloride containing phases (NaCl and $CaCl_2$). In addition, also CaO and remnant Si were found, probably in small amounts, based on the relative height of their peaks. These results are in line with the high calcium and chloride content found by the EDS and XRF analyses.

**Table 4**
Chemical composition of the waste silica sludge and reference micro-silica by XRF.

| Substance | Batch 1 (mass %) | Batch 2 (mass %) | Batch 3 (mass %) | Micro-silica (mass %) |
|---|---|---|---|---|
| $SiO_2$ | 80.58 | 40.67 | 43.09 | 96.12 |
| $Na_2O$ | 2.55 | 0.36 | 0.27 | 0.21 |
| $Al_2O_3$ | 8.86 | 1.50 | 1.37 | 0.86 |
| $Fe_2O_3$ | 0.39 | 0.41 | 0.47 | 0.34 |
| CaO | 1.96 | 55.79 | 44.51 | 0.39 |
| Cl | 0.56 | 1.86 | 1.34 | 0.30 |
| $P_2O_5$ | 3.22 | 0.02 | 0.03 | 0.07 |
| $K_2O$ | 0.14 | 0.13 | 0.11 | 1.05 |
| MgO | 0.15 | 0.75 | 0.60 | 0.53 |
| $TiO_2$ | 0.06 | 0.06 | 0.06 | 0.01 |
| MnO | 0.01 | – | 0.03 | 0.04 |
| $SO_3$ | 2.07 | 0.28 | 0.15 | 0.36 |
| Total C | 1.01 | 11.91 | 10.69 | 0.66 |

*3.1.3. Gravimetric (TG) and differential scanning calorimetry (DSC)*

To complement the characterization of the different silica sludge samples, a combined TG/DSC analysis was performed. Fig. 3a shows the mass loss over the temperature. It is evident from Fig. 3a that batch 1 is mainly composed of water (42 to 45%) and amorphous $SiO_2$. The temperature range between 20 and 200 °C, where this batch shows the main mass loss, is typically for hydroxylated colloidal silica, which is mainly used in the production of CMP slurries. The peak shown in Fig. 3b (131 °C) is related with zeolitic water (water inside the porous structure of the amorphous silica). In case of batches 2 and 3, the water content is lower than batch 1, but both samples have a main loss of weight between 420 and 750 °C. This loss of weight is caused by the de-carbonatation ($CO_2$ release) of the calcium carbonates. Taking into account the loss of mass (23–27% $CO_2$) and the molecular weight of each compound, it is possible to estimate that batch 2 and batch 3 have 56% and 49% of $CaCO_3$ respectively. Analyzing Fig. 3b, several observations can be made. Firstly, the peak where the water is released is related to the difference in the porous structure (explained in Section 3.1.4) and to the composition of both samples. The peaks corresponded to 131 °C to batch 1 and between 79.1 and 83.1 °C for batches 2 and 3. Secondly, the successive peaks for batches 2 and 3 are related to the de-carbonation of $CaCO_3$ (636.6 and 695.7 °C) and $MgCO_3$ (595.4 °C) and the consequent formation of CaO, which reacts later with the amorphous $SiO_2$ to form γ-$C_2S$ (739.3 and 756.7 °C).

*3.1.4. Nitrogen physical absorption (BET specific surface area) and density analysis*

The different adsorption curves obtained for the batches of silica sludge are presented in Fig. 4a. All samples show absorption curves of Type IV, as it is classified by the International Union of Pure and Applied Chemistry (IUPAC) [42]. These curves are typical for mesoporous powders. The calculated BET specific surface areas are: 178 $m^2/g$ for batch 1, 29 $m^2/g$ for batch 2 and 38 $m^2/g$ for batch 3 (Fig. 4b). These results are in agreement with the FEG-SEM, XRD and XRF analyses. In general, a larger content of nano-silica in the samples gives a larger specific surface area. The BET surface area calculated for batches 2 and 3 is comparable to the values specified for micro-silica in NEN EN 13263-1:2005 [39], where a value between 15 and 35 $m^2/g$ is given. Using the calculated BET specific surface area (Fig. 4b), the density of the particles (compare Section 3.1.5) and the procedure presented by [22], it was possible to determine the size of the primary particles in the different batches using Eq. (1). An average primary particle size computed for the different batches of silica sludge were: 16 nm, 84 nm and 66 nm for batch 1, batch 2 and batch 3, respectively.

*3.1.5. Specific density of the nano-silica sludge particles by helium pycnometry*

The results of the density measurements are depicted in Fig. 5 together with the density limit of commercial nano- and micro-silica

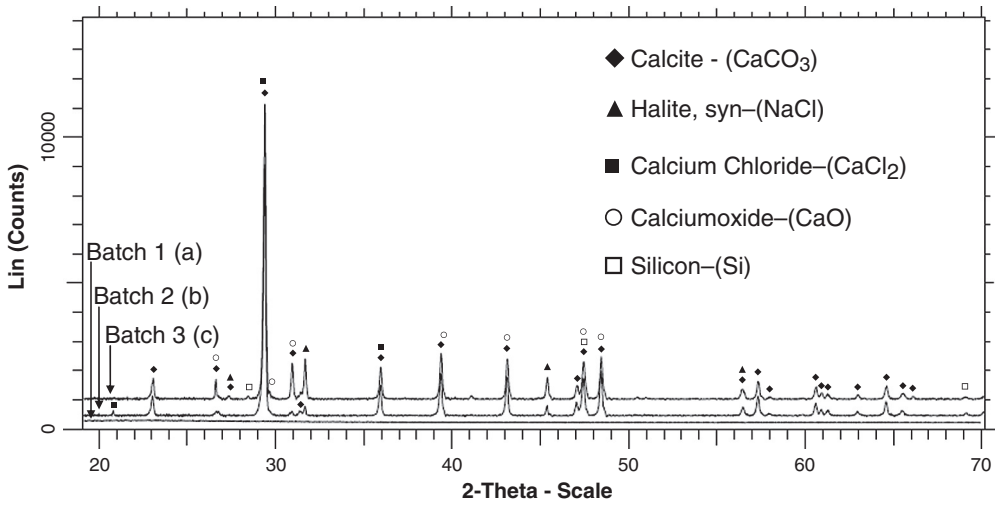


**Fig. 2.** XRD spectrums of the different batches of nano-silica sludge (with a filtered background).

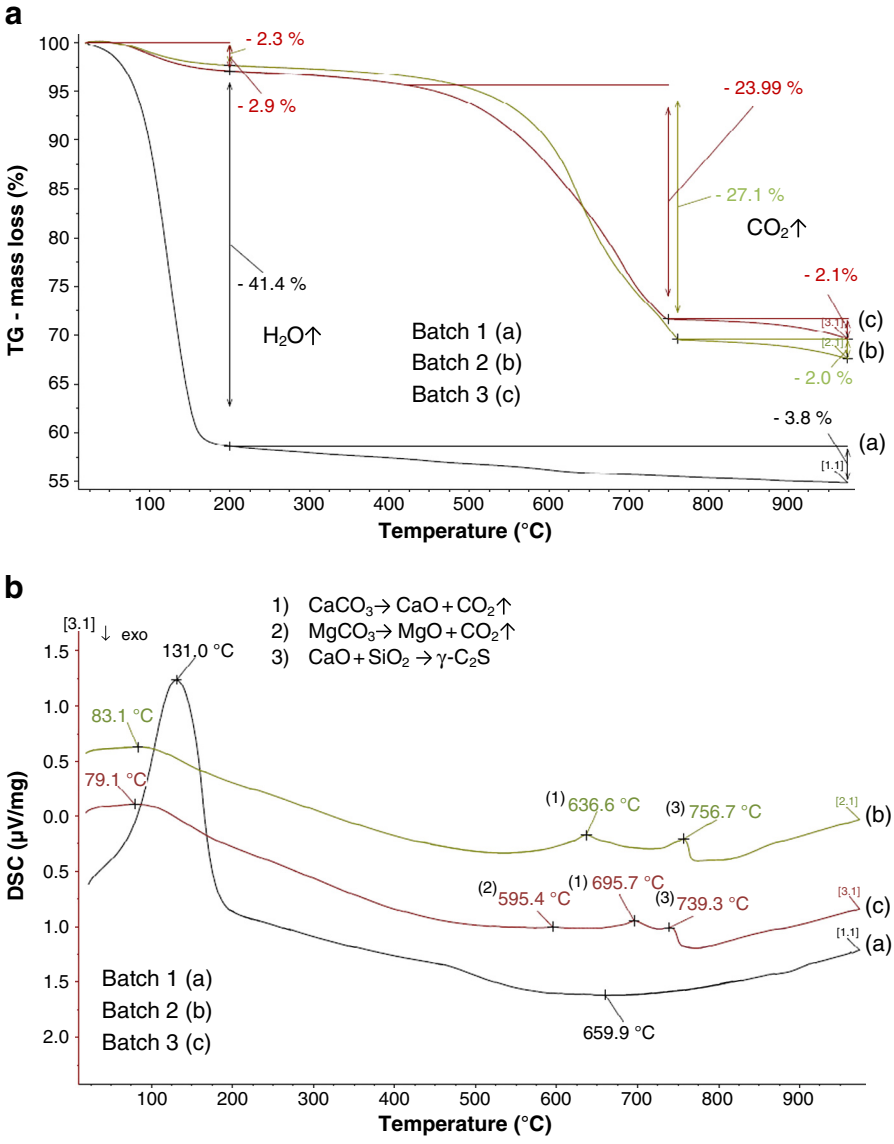


**Fig. 3.** TG/DSC curve for the different batches of nano-silica sludge, a) TG (sample mass loss in percentage), b) DSC (deferential scanning calorimetry).

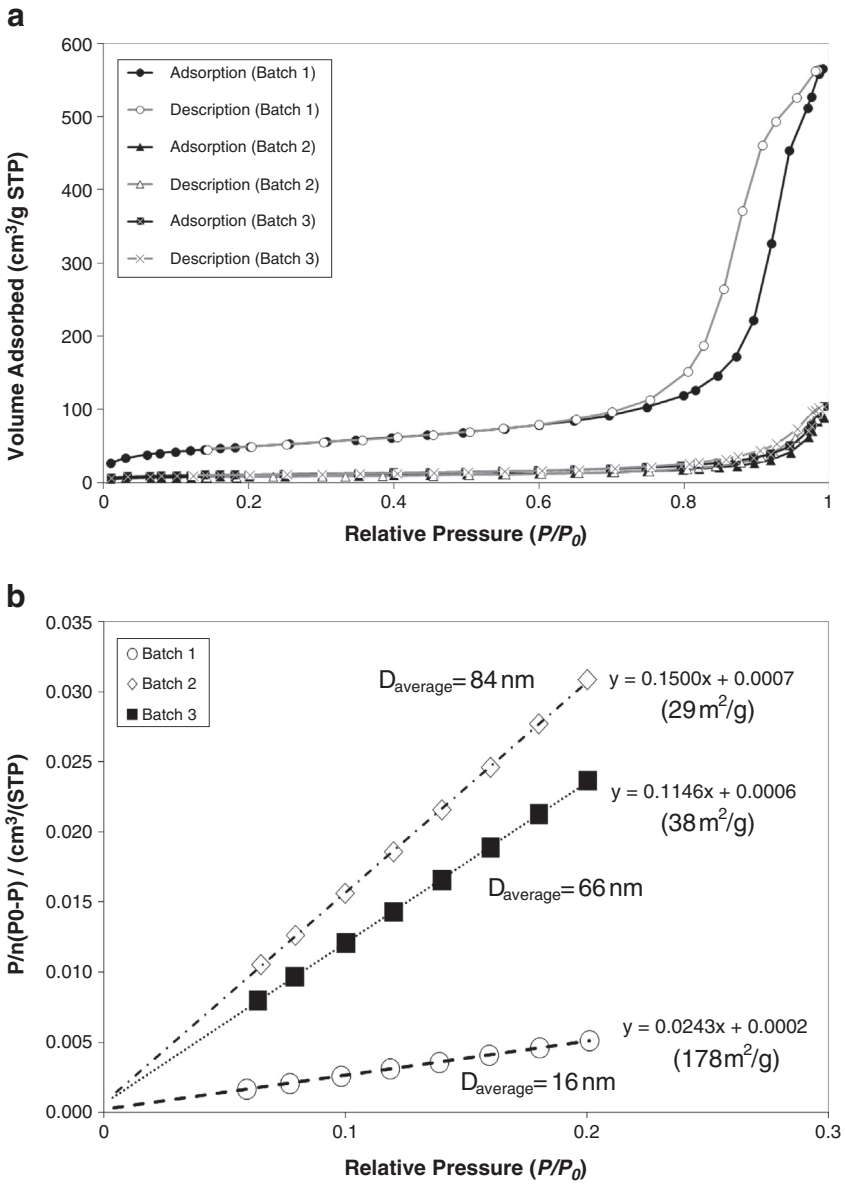


**Fig. 4.** a) Nitrogen adsorption/desorption isotherms for the different batches of nano-silica sludge, b) BET plot derived in the relative pressure range from 0.20 to 0.04.

powder [43]. In this context the nano-silica of batch 1 is the only sample with density values in the nano-silica range (average 2.17 g/cm$^3$). The other two batches presented specific densities higher than the specified limits for micro-silica (2.30 g/cm$^3$). The average values obtained were 2.45 g/cm$^3$ for batch 2 and 2.40 g/cm$^3$ for batch 3. The reason for the high density is the high content of $CaCO_3$, as discussed previously; batch 2 and batch 3 have 52 and 62 wt.% of $CaCO_3$, which density is about 2.73 g/cm$^3$.

### *3.2. Dispersability study with high shear energy mixer and zeta potential (ξ) measurements*

Due to the highly agglomerated state of the nano-silica sludge, a dispersability study was performed. For this study only a sample of batch 2 was considered based on the similarity to batch 3. Batch 1 was discarded for the dispersability studies due to its high content of impurities. In addition, zeta potential was measured to study the stability of the dispersion. The results of the performed tests are presented in Figs. 6 and 7. Comparing the results shown in Figs. 6 and 7, several observations and conclusions can be drawn. First, the size reducing effect or dispersion is more effective at 7000 rpm than at 3000 rpm. In the latter case, an effective reduction was observed after the first 30 min of stirring, but with proceeding stirring time, only the coarse particles (D(0.9) parameter) were affected, whereas the other two parameters (D(0.5) and D(0.1)) showed a constant value over that period. The same behavior was also confirmed by the constant values of the surface weighted mean, shown in Fig. 6b. It is evident that the introduced energy was not sufficient to break the agglomerated particles to nanoparticles and to totally disperse them. The maximum amount of nanoparticles generated during the studied period was 14.5% by volume. Similar trends were obtained with the experiments at 7000 rpm (Fig. 7). Even though more energy was introduced into the system, only D(0.9) and D(0.5) are effectively reduced. The higher mixing energy results in more nanoparticles at shorter time. During the first 30 min, almost the same amount (by volume) of nanoparticles was generated at 7000 rpm as generated at 3000 rpm during 210 min. The maximum amount of nanoparticles generated at 7000 rpm was 22% by volume. This behavior has already been reported by different authors [44–47]. In general, larger agglomerates suspended in a fluid are broken when the hydrodynamic forces exceed the cohesive bonds between particles

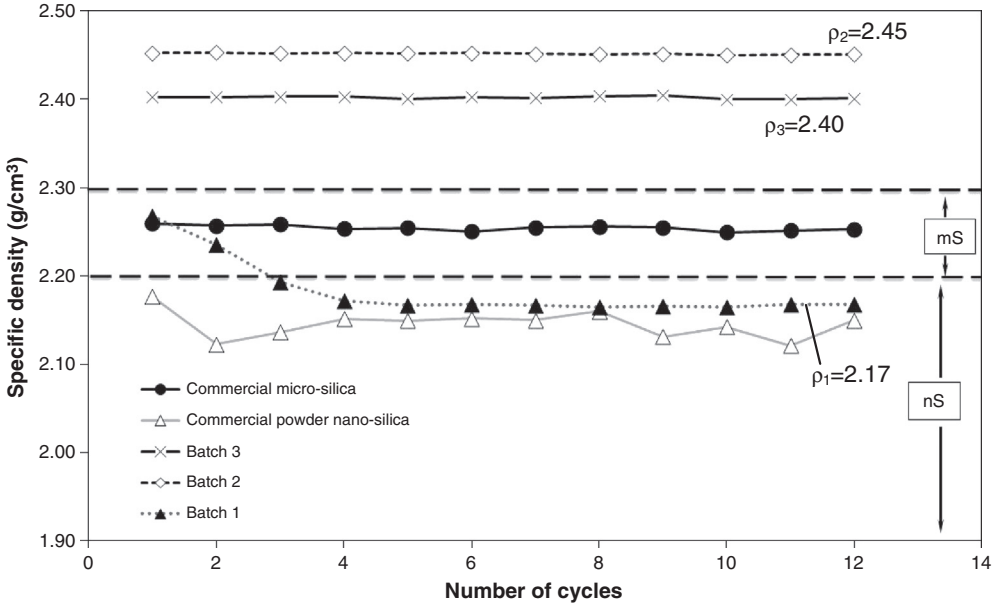


**Fig. 5.** Specific densities of the different batches of nano-silica sludge versus the number of measured cycles.

or smaller agglomerates. The strength of individual bonds depends on the type of nanoparticles (van der Waals interactions), surface properties (wettability, zeta potential, etc.) and the nature of the dispersion media (liquid bridges within agglomerates). Different mechanisms of fracturing have been postulated (shattering, rupture and erosion) and their occurrence depends on the size of the agglomerates and the energy introduced to the dispersion [45]. It has been postulated that erosion occurs at low energy intensity and that particles are broken by fragmentation when the energy intensity increases [48]. As the agglomerates become smaller during de-agglomeration, surface forces become more important than mass forces and for agglomerates smaller than 1 μm, surface forces are more than one million times larger than mass force [49] (see, Fig. 8). Therefore, fracturing of large agglomerates is relatively simple, whereas fracturing of agglomerates smaller than 1 μm might be very difficult and it has been suggested that the particles smaller than 10 to 100 nm cannot be broken by mechanical action [50]. Probably, it is the case of the nano-silica sludge particles. It was easy to break the bigger agglomerates (decreasing of D(0.9) and D(0.5)), but the smaller ones (D(0.1) and particles lower than 1 μm) reached a constant value earlier (see, Fig. 7a). Based on these results, it can be concluded that the breaking mechanism is dominated by the erosion and rupture of the bigger agglomerates. In addition, it is evident that the energy introduced in the system (7000 rpm) and the time of stirring were not enough to produce shattering of the agglomerates to nano-particles. It is recommended to perform further research using another type of mechanical mixing technique or increase the stirring time to more than 210 min.

Other researchers reported [44,46,51] that the mechanical stirring should be complemented with chemical additives to increase the dispersability and to overcome the forces involved when small agglomerates are generated during the dispersing process. For that reason, experiments with varying pH values of the dispersion were performed. The results for varying pH values of the dispersion between 7.8 and 9.6 were similar (Fig. 9), only a small increase in the volume of nanoparticles was observed. Nevertheless, the dispersion shows more stability over time and less sedimentation of the particles was observed after 3 days. The zeta potential of the silica particles dispersed using the high-energy mixer is shown in Table 5. Studying the results presented in Table 5, it is evident that it is easier to disperse the silica sludge of batch 2 due to the higher zeta potential (−39.3 mV). It can be stated that with higher pH value, the particle surfaces are more negatively charged [52]. A more negative zeta potential produces more stable dispersions due to the electrostatic repulsion of the particles, which avoids their re-agglomeration. The higher zeta potential improves the stability of the particles smaller than 1 μm. Despite of the higher stability, it is still not possible to increase the volume of dispersed nano-particles to more than 22% (Fig. 9b).

### 3.3. Hydration kinetics of cement pastes with nano-silica

Studying the obtained curves (Fig. 10a), it is evident that the replacement of cement with different amounts of nSS of batch 2 does not have a decreasing effect on the heat flow of the blended paste. On the contrary, a higher heat flow was found due to the nucleation effects produced in the cement paste and due to the pozzolanic activity promoted by the presence of amorphous nano-silica and $CaCO_3$ particles (Fig. 10b). Different authors reported [6,53–56] that nano-particles can accelerate the setting of cement pastes due to two acting mechanisms. The first one is the so-called filler effect that appears when the nano-particles are inert. Fillers with very high specific surface area produce more nucleation points for C–S–H seeds at early age. When the thermodynamic barrier is exceeded, these nuclei start to grow and to form second stage C–S–H gel and portlandite [57]. The second effect is routed to the reactivity of the nano-particles in the case of amorphous $SiO_2$. The small amorphous $SiO_2$ particles react with the CH released from the hydration of the calcium silicates in the clinker forming extra C–S–H gel. Similarly, it is stated that part of the $CaCO_3$ is reactive [58] and it can be incorporated in the hydration products from the aluminate phases (ex. AFm or AFt) [6,58]. These two effects are probably acting at the same time producing the extra heat observed when the concentration of batch 2 silica sludge is increased. Another observation can be made from Fig. 10a. It is possible to observe that higher amounts of silica sludge batch 2 produce the appearance of a second peak (indicated by a black arrow at 30 h in Fig. 10a). Normally, this peak appears at about 30 h of hydration and can be attributed to the formation of monosulfoaluminate phases (AFm) [57,58] due to the reaction between the initial ettringite (AFt) formed at early age and the remnant $C_3A$. Likewise, it can be also caused by the formation of manocarboaluminate ($CO_3$–AFm) as it was stated by other authors [6,58] for OPC–$CaCO_3$ blends. The accelerating effect of the silica sludge batch 2 is evident from Fig. 11a. In this figure, it is possible to observe that the rate of heat (increasing slope) in the acceleration period follows a linear relationship

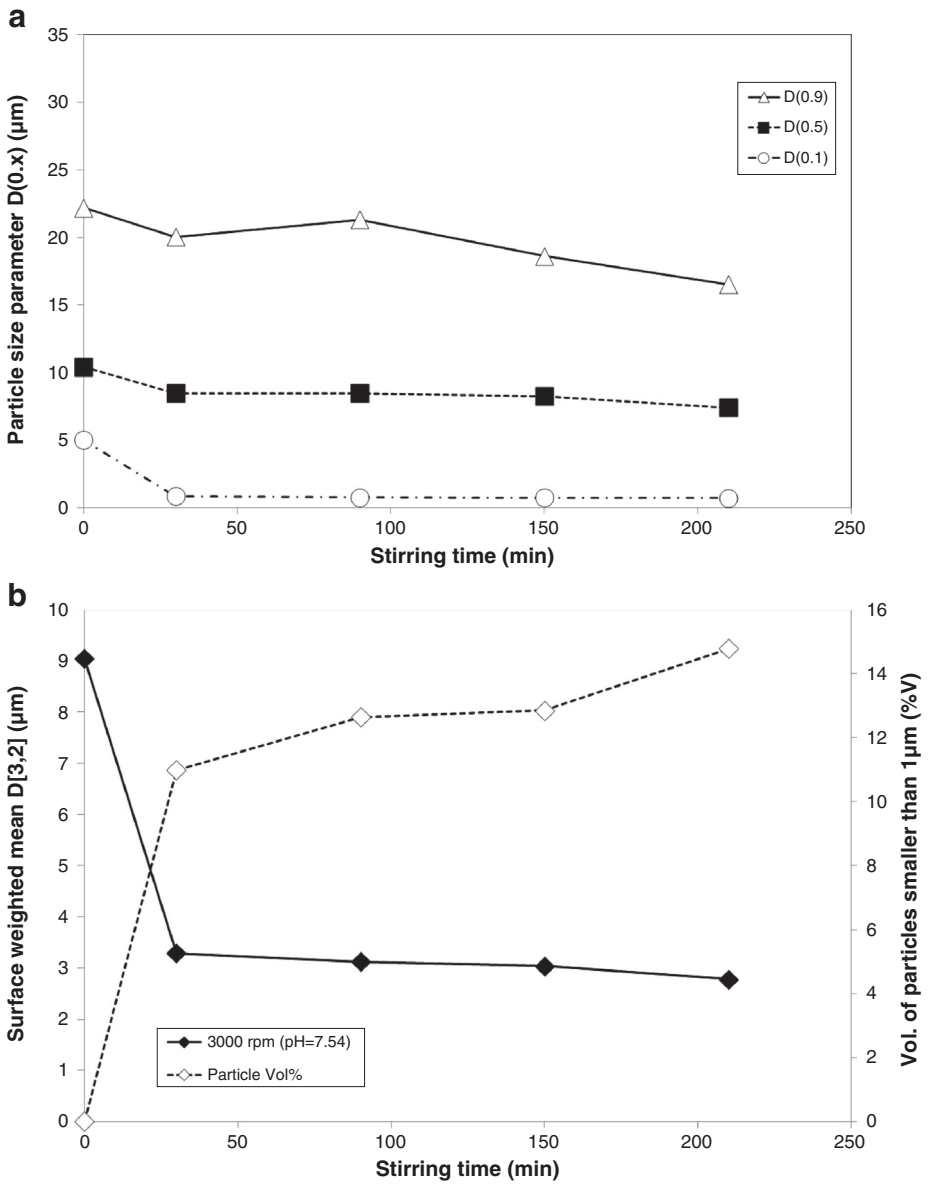


**Fig. 6.** a) Evolution of the granulometric parameters of one nano-silica sludge (batch 2, 3000 rpm over 210 min, pH = 7.54), b) surface weighted mean (D[3,2]) and volume (%) of nanoparticles generated.

($R^2 = 0.99$). It is possible that the slope of this period is related to the increased amount of nucleation sites produced by the increased specific surface area.

Despite of the accelerating effect described before, the presence of SP in the silica sludge caused an extension of the dormant period (Fig. 10a and Table 6). The increasing amount of batch 2 nSS slurry increases the total SP content as well (see Table 2). Despite the retardation effect on the dormant period (calculated as the time between the lower point of the heat flow curve and the first inflection point in the main peak), the relative setting time (calculated as the time between the first and the second inflection point in the heat flow curve), as well as the time to reach the maximum hydration peak of the cement paste, were accelerated. The pozzolanic activity of the silica sludge batch 2 is confirmed by the presence of an increase of the total heat shown in Fig. 10b. The total heat is the contribution of heat produced by the cement particles themselves (accelerated by the filler addition) and the heat contribution of the pozzolanic reaction between the nano-silica particles and the precipitated $Ca(OH)_2$ [58]. The total heat can be related to the hydration degree of the paste ($\alpha = Q(t)/Qmax$) [59]. Similarly, the hydration degree of the paste was related to the compressive strength of the paste, if the parameters of the microstructure are similar (ex. porosity). Thus, higher compressive strength is expected with the progressive increase of nano-silica sludge. In contrast to the rate of heat evolution during the acceleration period, the maximum extrapolated heat ($Q_{max}$) follows an exponential trend (Fig. 11b) with a good correlation ($R_2 = 0.96$).

As an additional hydration kinetic study, cement pastes following the recipe shown in Table 3 (without sand) were tested by isothermal calorimetry. The purpose of this test was to compare the effect of the different silica sludge batches (1–3) at the same replacement level (7% bwoc) and comparable workability (adjusted by different SP amount) on the hydration kinetics of the standard mortars. The resultant heat flow and accumulative heat evolution curves are shown in Fig. 12. In Fig. 12a, it is possible to observe that the silica sludge of batch 1 presented, at the initial 24 h of hydration, a lower heat flow but a wider peak compared to the pure cement paste. These differences can be attributed to several factors. The first influencing factor is related to the delaying effect due to the presence of SP in the paste of batch 1 (0.68% bwoc). Nevertheless, the delaying effect of the SP normally

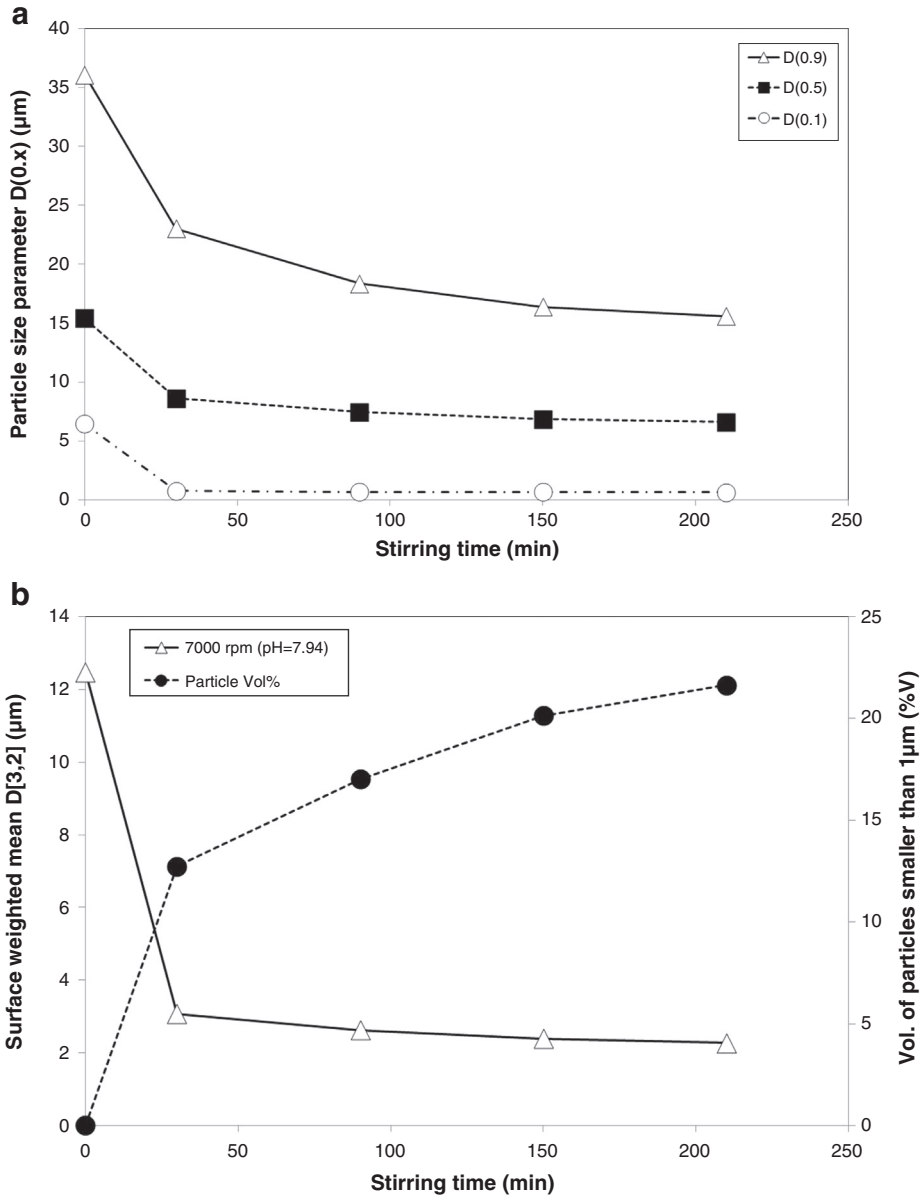


**Fig. 7.** a) Evolution of the granulometric parameters of one nano-silica sludge (batch 2, 7000 rpm over 210 min, pH = 7.94), b) surface weighted mean (D[3,2]) and volume (%) of nanoparticles generated.

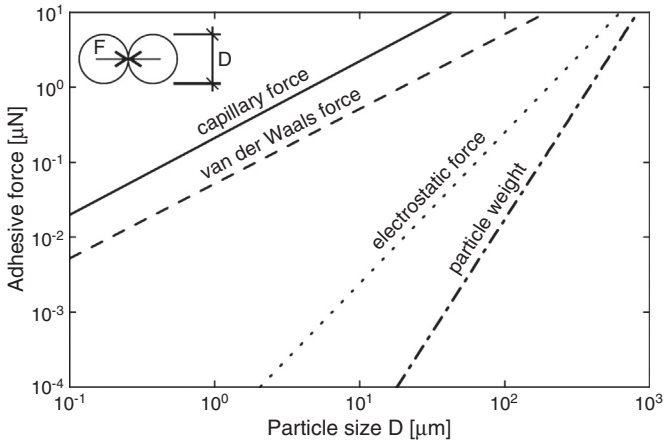


**Fig. 8.** Interparticle forces of spherical particles and particle weight in dependence of the particle diameter [71].

influences the dormant period (as it is evident from Table 7) but will not change the height of the maximum peak of hydration. A change in the maximum peak height is normally expected with retarding agents instead of PCE type superplasticizer [60]. This leads to a second possible factor that could produce the reduction in the hydration peak. The second factor should be the precipitation of initial hydration products, supported by a higher heat during the initial dissolution of the pastes (initial 2.5 h), or the adsorption of some contaminants such as unknown organics or water-soluble phosphates (batch 1 has 3.2% of $P_2O_5$) on the surface of the cement grains with some protective properties producing a retarding effect in the rate of Alite hydration. Thus, the hydration rate is reduced (see Fig. 13a), but extended in time (widening the hydration peak). The widening of the hydration peak is also the result of the higher rate of hydration in the aluminate phases. Different authors [58,60] reported that a small amount (0.05%) of water-soluble $P_2O_5$ or organophosphonates produces setting retardation. The mechanism reported [60] involves the adsorption of phosphonate groups onto the nuclei of cement hydrates, thus hindering their growth. Even though

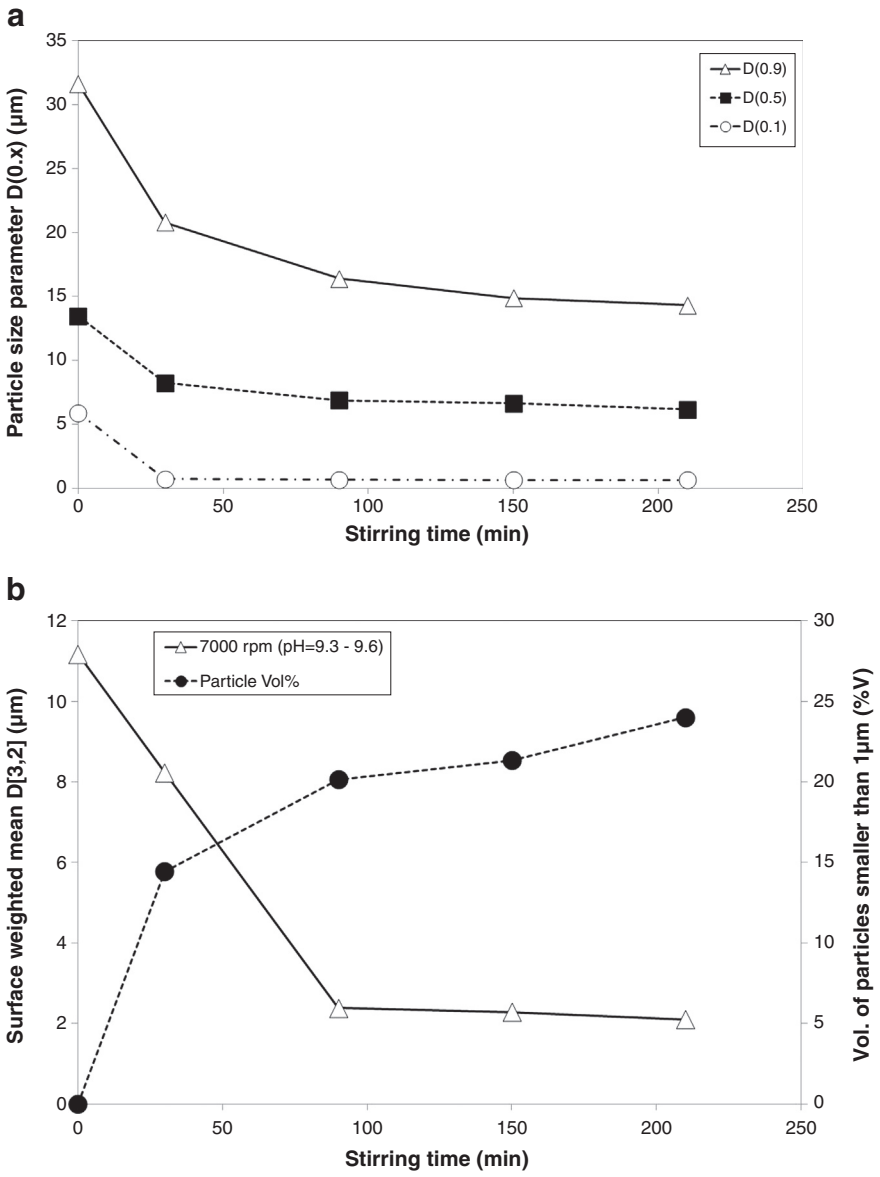


**Fig. 9.** a) Evolution of the granulometric parameters of nano-silica sludge (batch 2, 7000 rpm and 210 min, pH = 9.6), b) surface weighted mean (D[3,2]) and volume (%) of nanoparticles generated.

a lower heat flow was observed in pastes with the silica sludge of batch 1, the accumulative heat is similar at 78 h of hydration (Fig. 12b) and the extrapolated maximum heat becomes higher than for cement, but lower than that of the other silica sludge batches (2–3), as it is shown in Fig. 13b. The lower heat flow observed is not expected because the silica sludge of batch 1 has the highest BET specific surface area (178 $m^2/g$), thus a higher filler and pozzolanic effect are expected to produce an increase in the heat flow curve compared to the reference cement paste and the other silica sludge batches (with BET of 29–38 $m^2/g$).

Contrary to the silica sludge of batch 1, batches 2–3 presented higher heat flow than the cement paste, but similar to the reference micro-silica studied. The main differences observed are the heat released during the first hours and the height of the second hydration peak related to the aluminate phases. This is attributed to the different amount of $CaCO_3$ estimated (Section 3.1.3) in the silica sludge of batches 2–3 (56 and 49%, respectively). The higher amount of $CaCO_3$ (lower $SiO_2$) of the silica sludge of batch 2 influenced in more extent the aluminate hydration peak mainly due to the filler and pozzolanic effect explained before. The small difference in the composition is also observed in Fig. 13a where the silica sludge of batch 2 shows a slightly lower rate of hydration (slope) during the acceleration period due to its lower content of $SiO_2$ compared to batch 3. Both silica sludges (batches 2–3) are characterized by slightly higher rate of hydration (slope during the acceleration period) compared to the reference micro-silica (Fig. 13a). It is caused by the higher BET specific surface area of the silica sludges (29, 38 and 22 $m^2/g$ for batch 2–3 and micro-silica, respectively). Also, the differences in the composition influenced the estimated dormant period, relative setting time and the time to reach the maximum peak of hydration as it is shown in Table 7. In general, a higher amount of $SiO_2$ with the same SP content (0.44% bwoc) produced shorter dormant

**Table 5**
Zeta potential of the nano-silica of batch 2 dispersed in tap water (1 wt.%) at 25 °C.

| Sample | Zeta potential (mV) |
|---|---|
| Silica sludge 3000 rpm pH = 7.4 | −26.1 |
| Silica sludge 7000 rpm pH = 7.8 | −26.6 |
| Silica sludge 7000 rpm pH = 9.6 | −39.3 |

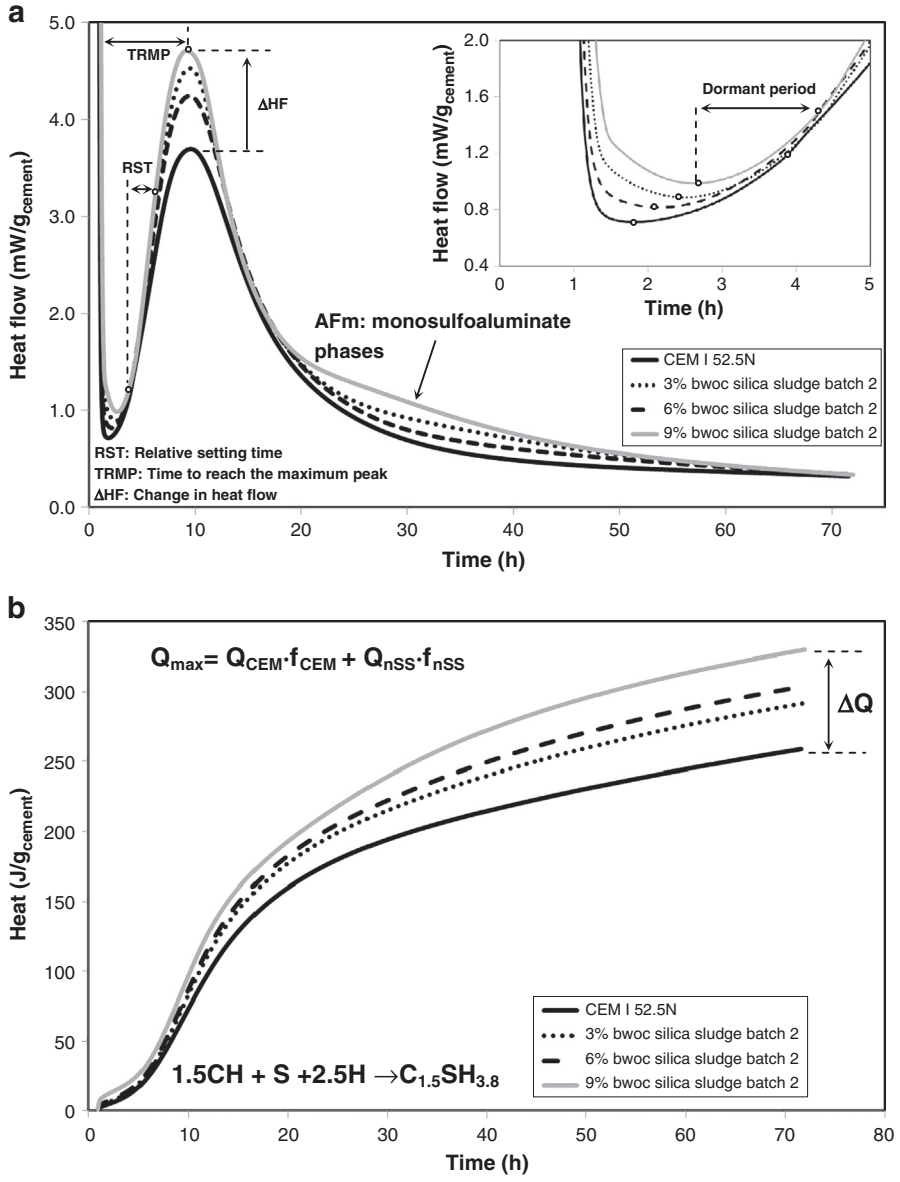


**Fig. 10.** a) Normalized heat flow of cement pastes with batch 2 nSS addition (bwoc) and details of the different stages of the dormant period, b) normalized total heat evolution of cement pastes (Q) with batch 2 nSS addition (bwoc).

period and setting times for the silica sludge of batch 3. Nevertheless, it does not apply for the micro-silica slurry (96% of $SiO_2$ and 0.24% bwoc of SP), which shows a longer dormant period and the time to reach the maximum hydration peak (see, Table 7).

Fig. 13b shows the maximum extrapolated heat for the different pastes with 7% cement replacement. The cementitious properties of the different silica sludge batches are confirmed by the presence of an increase of the total heat compared to the cement reference. The total heat is the contribution of heat produced by the cement particles themselves (accelerated by the filler addition) and the probable heat contribution of the pozzolanic reaction between the nano-silica particles and the precipitated portlandite [58]. A further analysis is presented in Section 3.5.

### *3.4. Compressive strength tests of cured cement mortars and pozzolanic activity*

The evolution of the mechanical properties of the different mortars tested is shown in Fig. 14. Analyzing the evolution of the flexural strength over time (Fig. 14a), several observations can be made. At early age (1 day) the flexural strength was influenced by the different doses of SP added to the mortar (see Table 3). The nano-silica of batch 1 showed the lowest flexural strength due to the high content of SP (0.68%) and probably due to differences in their chemical composition and the presence of contaminants. On the contrary, batches 2 and 3 showed already at 1 day comparable flexural strength than the reference standard mortar (CEM I 52.5 N). At 7 days, the same behavior in the flexural strength was observed for all tested mortars, with the exception that the difference in the strength of batch 1 to the reference mortar is smaller. Finally, at 28 days all tested mortars obtained lower flexural strength than the reference mortar. It is important to notice that all 28 days average flexural strength values are near to the error band of the test (±8.3%).

In case of the compressive strength of the tested mortars (Fig. 14b) at 1 day, it is also possible to observe the influences of the different SP concentration. At this age, the mortar prepared using the nano-silica of batch 3 showed the highest compressive strength. In addition, the nano-silica of batch 1 presented the lowest compressive strength —

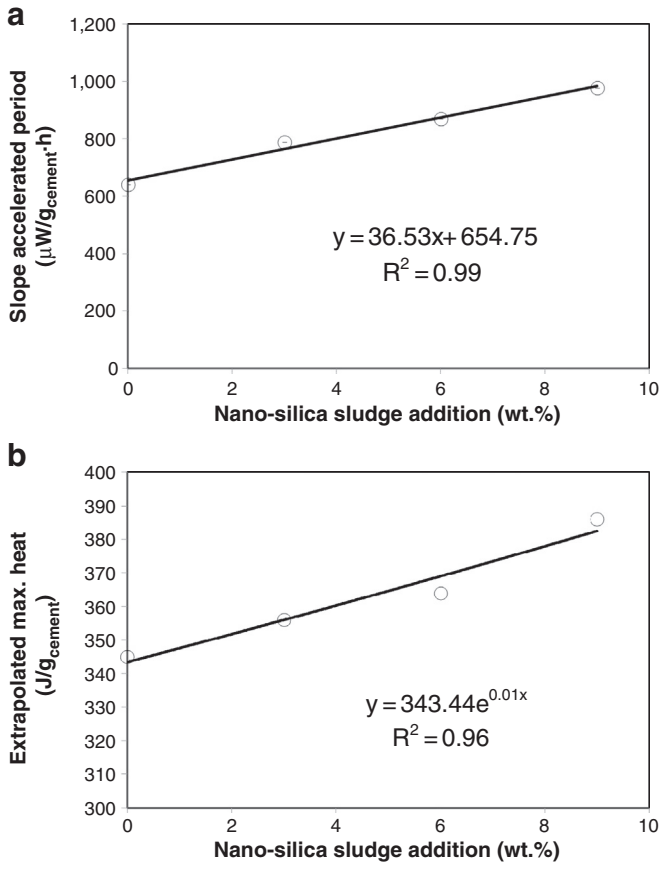


**Fig. 11.** a) Changes in the slope of the accelerated period caused by the addition of nSS (data were derived from the curves of Fig. 9a, b) changes in the extrapolated maximum heat of cement paste with nSS (derived from the curves of Fig. 9b taking into account an exponential fit decay model).

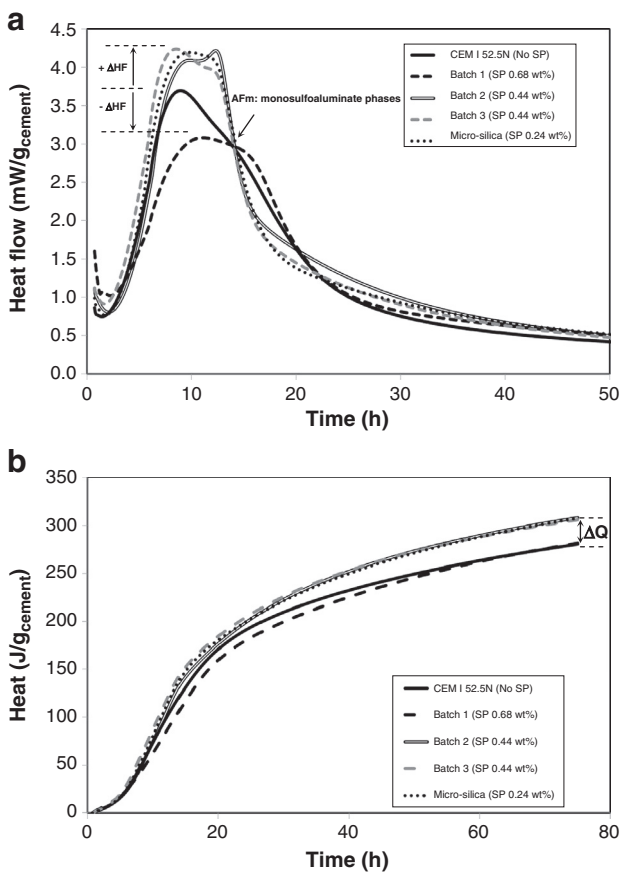


**Fig. 12.** a) Normalized heat flow of cement pastes with 7% bwoc of nSS and different SP content, b) normalized total heat evolution of cement pastes (Q) with 7% bwoc of nSS and different SP content.

(similar to the flexural strength). The lowest compressive strength of the silica of batch 1 is the result of its $P_2O_5$ content. The 1 day compressive strength results are in line with the calorimetric curves shown in Fig. 12a. At 7 days, the strength development of the samples of batches 2, 3 and the reference micro-silica reached higher compressive strength than the reference mortar (CEM I 52.5 N). At this age, the delaying effect observed for the silica sludge of batch 1 is still evident. Finally, at 28 days the compressive strength of the mortar with nano-silica of batch 3 resulted in higher compressive strength than the mortar with 100% cement (CEM I 52.5 N), but lower than the micro-silica mortar. At this age, the mortar prepared with silica sludge of batch 1 showed the lowest compressive strength (60 N/mm$^2$). Apparently, at 28 days the delaying effects produced by the $P_2O_5$ content in batch 1 are overcome and the mortar developed its normal strength. Another factor to take into account in the compressive strength results is the volume of air voids of the mortars which influences the final compressive strength. In general, it is empirically accepted that 1% increase in air void volume will lead to a 5% decrease in compressive strength [61]. Table 3 shows the estimated air void content of the hardened mortars. The data listed in Table 3 reveal that the mortar with the highest air void content was batch 1 (11%) and the lowest value was obtained by the mortar with micro-silica (4%). The difference in the air void content helps to explain why the silica sludge of batch 1 presented the lowest compressive strength despite of its highest specific surface area. The methodology used to obtain the mechanical properties of the mortar can be validated comparing the specified values of the cement (CEM I 52.5 N) as published in the ENCI "Betonpocket 2010" [62] (1 day 22 ± 3 N/mm$^2$ and 28 days 65 ± 4 N/mm$^2$). In this case, the experimental values obtained are in the range reported for this type of cement produced in the ENCI manufacturing facilities of Maastricht, The Netherlands.

**Table 6**
Hydration kinetics of cement pastes containing nano-silica of batch 2.

| Paste type | Dormant period (h:min) | Relative setting time (h:min) | Peak time (h:min) |
|---|---|---|---|
| CEM I 52.5 N | 0:39 | 2:03 | 7:39 |
| 3% bwoc nSS batch 2 | 1:03 | 1:56 | 7:20 |
| 6% bwoc nSS batch 2 | 1:22 | 1:45 | 6:58 |
| 9% bwoc nSS batch 2 | 1:35 | 1:40 | 6:35 |

**Table 7**
Hydration kinetics of cement pastes containing 7% bwoc of the different samples studied.

| Paste type | Dormant period (h:min) | Relative setting time (h:min) | Peak time (h:min) |
|---|---|---|---|
| CEM I 52.5 N (No SP) | 0:42 | 2:10 | 8:47 |
| Batch 1 (SP 0.68%) | 1:32 | 1:31 | 10:48 |
| Batch 2 (SP 0.44%) | 1:49 | 2:01 | 9:38 |
| Batch 3 (SP 0.44%) | 1:29 | 1:51 | 8:19 |
| Micro-silica slurry (SP 0.24%) | 1:41 | 1:58 | 9:32 |

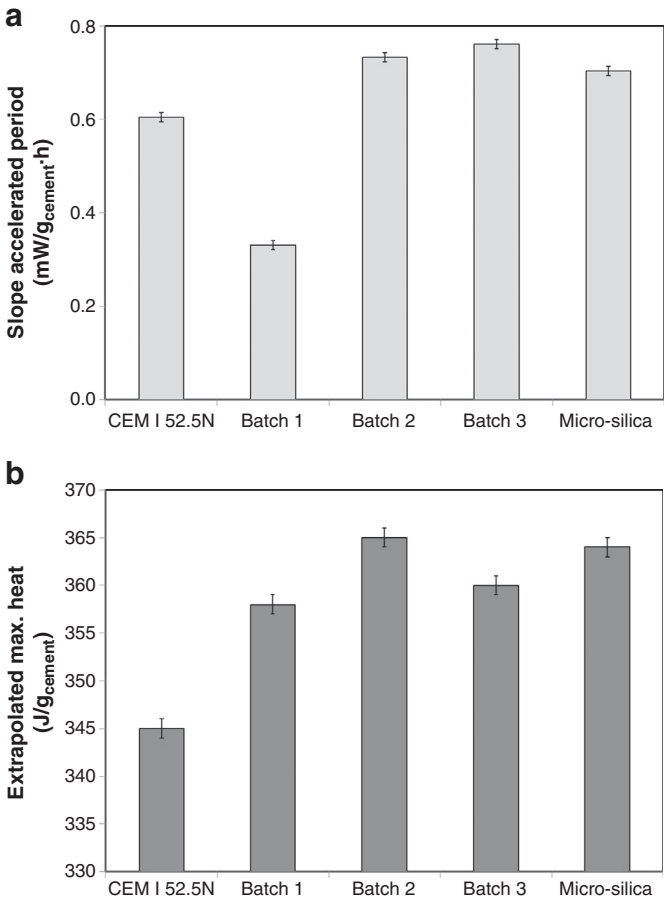


**Fig. 13.** a) Changes in the slope of the accelerated period caused by the addition of 7% bwoc of nSS and different SP amount, b) changes in the extrapolated maximum heat of cement paste with 7% bwoc of nSS and different SP content. The data were derived from the curves of Fig. 12a and b.

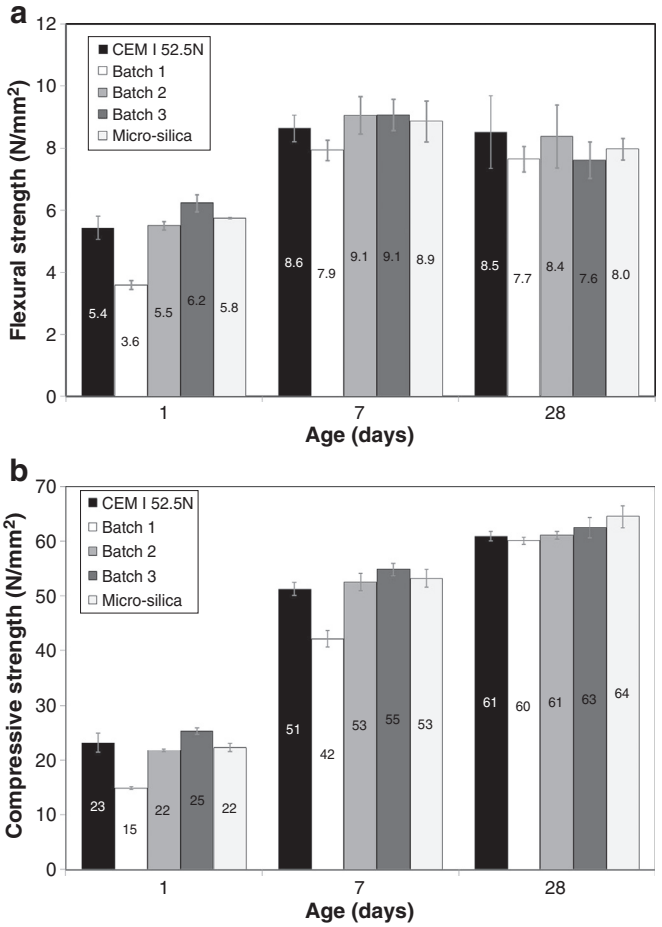


**Fig. 14.** Development of the mechanical properties of the tested mortars (7% nSS bwoc), a) flexural strength, b) compressive strength.

The values of the 7 and 28 days compressive strength were used to estimate the relative pozzolanic activity index of the different nano-silica and the micro-silica sample. The pozzolanic index was calculated based on the compressive strength of the reference mortar (100%) and is shown in Fig. 15. The computed activity index demonstrated that the nano-silica sludge has pozzolanic activity and confirms the results obtained by the isothermal calorimetric measurements. The activity index varied between 82 and 107 for all silica samples. Only the mortar with the silica sludge of batch 1 showed an index lower than 100%. On the contrary, the mortars with silica sludge of batches 2 and 3 presented a pozzolanic activity index of 100–103%. In general, the minimum pozzolanic activity index specified for micro-silica is 95 (lower limit) [39], this means that it is possible to classify the nano-silica sludge as a pozzolanic material like the micro-silica tested. Even though positive results were obtained, further research is needed to guarantee a constant quality of the nano-silica sludge due to the variations that were observed for the analyzed different batches. Furthermore, extra tests should be performed to determine the maximum amount of cement replacement that can be realized by the application of this type of waste nano-silica.

### 3.5. Characterization of the hydrated mortar

#### 3.5.1. Microstructural characterization and analysis

Fig. 16 shows an overview of the matrix and sand distribution of the hardened mortars. The microstructural characteristics of the mortars were found to be similar. The main differences observed were in the air void content and the narrow pore size distribution. It is expected because of the varying air void content of the mortars. The highest value was measured for batch 1 (11%) and the lowest for the micro-silica (4%), as it is shown in Table 3. Nevertheless, from a microstructural point of view, the mortars prepared with batch 1 and micro-silica presented a denser and lower porous interphase than the cement sample (Fig. 16e and f). On the contrary, in batch 2 more small pores were

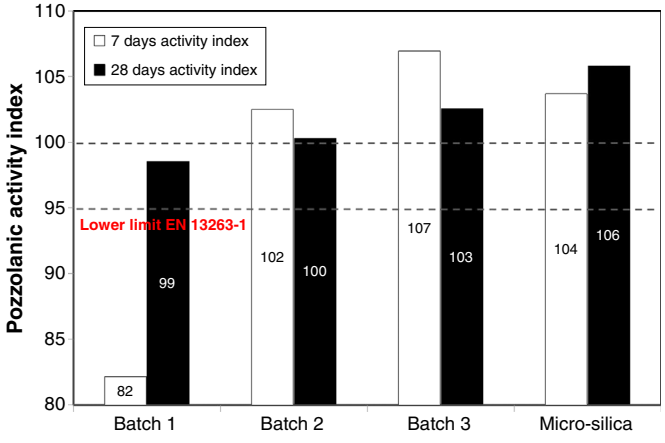


**Fig. 15.** 7 and 28 days pozzolanic index of the different nSS slurries tested.

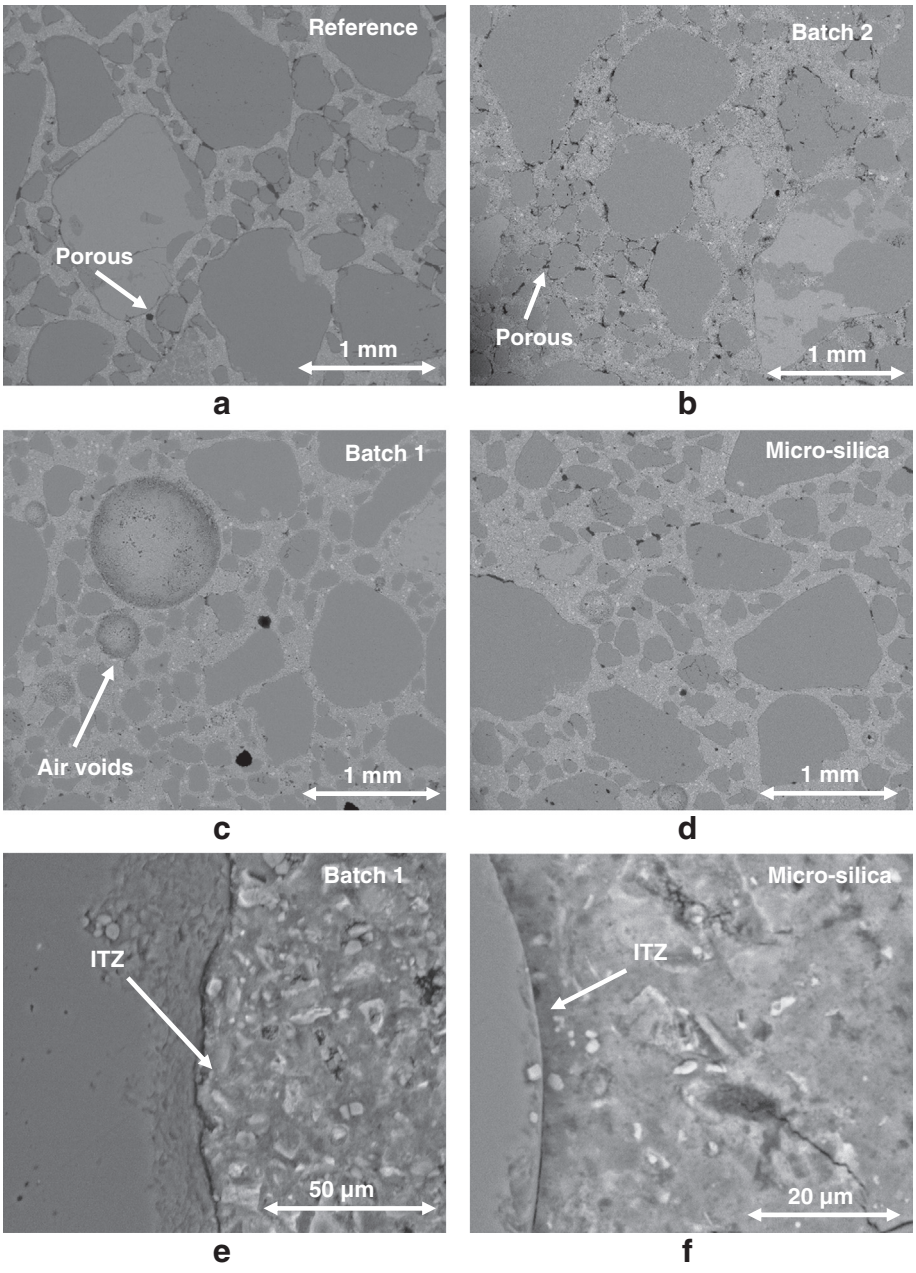


**Fig. 16.** ESEM–BSE pictures of different mortars tested at 28 days, a) reference, b) batch 2, c) batch 1, d) micro-silica, e) detailed ITZ in batch 1 mortar and f) detailed ITZ in micro-silica mortar.

observed in the sand grain interphases. In addition, only the mortar formulated with silica sludge of batch 1showed big unreacted agglomerates that are rich in iron (verified by EDS). Despite the presence of big agglomerates, the hardened matrix looks denser, probably due to a higher degree of hydration caused by the presence of amorphous silica particles with high specific surface area. In the following sections more evidence will be provided about the different effects of the silica sludges.

*3.5.2. Phases composition of the hydrated mortars by TGA/DTG and XRD*

The extent of cement hydration was estimated from changes observed by TGA/DTG and relative changes in the peak intensities of the crystalline phases in the XRD patterns. The results of thermogravimetric analysis are summarized in Fig. 17a and Table 8. For the interpretation of TGA/DTG results shown in Fig. 17a, it has been reported [57,58,63] that the mass loss at 100–130 °C corresponds to the evaporation of adsorbed water, at 115–125 °C to C–S–H gel, ettringite at temperatures of 120–130 °C, AFm phases at 180–200 °C, calcium hydroxide (portlandite) in the range of 410–550 °C and calcium carbonate at 680–750 °C. In addition, a presence of a broad initial peak, related to a $CO_2$ release at 550–680 °C has been attributed as an indication of the formation of significant fraction of calcium manocarboaluminate [64]. When comparing the mass loss in the different mixtures, four differences can be observed. Firstly, the initial shoulder presented at the temperature range of 85–115 °C disappeared in the case of the silica of batch 1 and becomes more noticeable in the case of the micro-silica mortar. Secondly, the main peaks attributed to the portlandite amount in the mortars are low compared to the peak of the reference mortar. This is caused by the pozzolanic reaction produced by the presence of amorphous $SiO_2$ in the silica sludge (batches 1–2) and the micro-silica

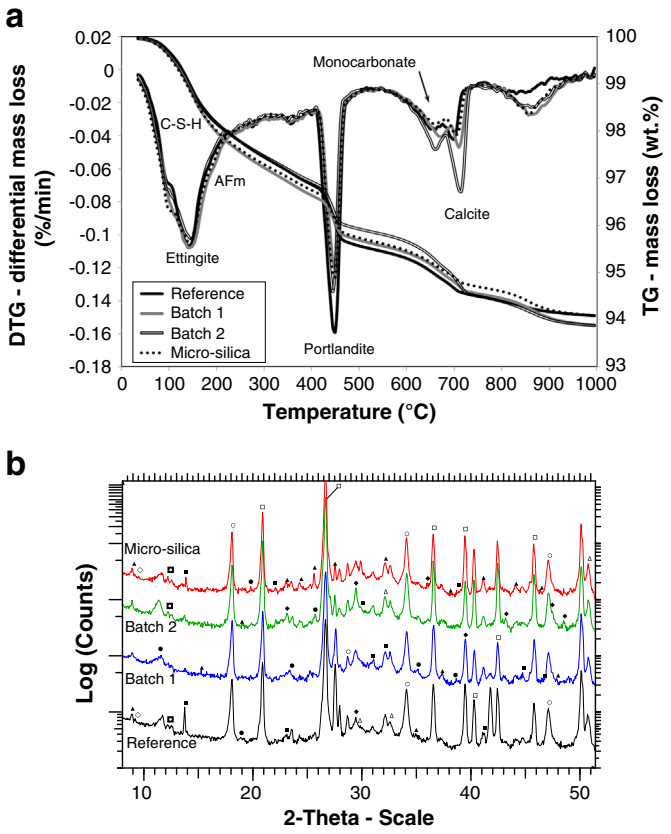


**Fig. 17.** a) TGA/DTG of the mortar studied, b) 28 days XRD spectra for the tested mortars, ■ alite, Δ belite, ◘ ferrite, ♦ calcite, □ α-quartz, ○ portlandite, ▲ ettringite, ◊ calcium monosulfoaluminate and ● calcium monocarboaluminate.

slurry. Thirdly, the two peaks related to the monocarboaluminates and calcite decomposition are different. The height of these two peaks depends on the initial $CaCO_3$ content of the cement and silica sludge of batch 2. One interesting observation is the fact that both peaks are shifted to the right for the case of batch 1. This is an evidence of the refinement of the microstructure due to a higher degree of hydration. Finally, the last difference is observed for the peak at 750–930 °C, which is bigger in the presence of the silica sludge and micro-silica. Unfortunately, no direct explanation of this extra mass loss was found in the literature. This peak is related to the decomposition of other unknown remnant phases (sulfates or other hydrates) that are formed due to the refinement of the C–S–H gel caused by the promoted pozzolanic reaction between silica nano-particles with high specific surface area. Evidence for this is that the peak is higher for the samples with more surface area and amorphous silica content. The quantitative results calculated by the mass loss and stequiometric considerations are shown in Table 8. For the data presented in Table 8 it is evident that the portlandite content is considerably decreased (34–35% average) for batch 1 and micro-silica mortars. The decrease is low (28%) for batch 2. The results demonstrated that the silica sludge (batches 1–2) poses supplementary cementitious properties. In addition, the calculated chemically bound water that gives indication about the hydration degree of the mortar's cement matrix is high in the presence of batch 1 and micro-silica. On the contrary, batch 2 presented lower amount of chemically bound water. It can be attributed to dilution effects (less cement content) and lower reactivity due to its diminished content of $SiO_2$ (40.7%). Similarly, the final calcite content varied depending on the sludge composition. The lowest values were found for the samples with higher amount of $SiO_2$ (batch 1 and micro-silica). It is possible that the promotion of the hydration due to the filler and pozzolanic effect increases also the partial reactivity of $CaCO_3$ (formation of mono and hemicarboaluminate phases) [6].

**Table 8**
Results of thermogravimetric analysis of the studied standard mortars.

| Mortar | Portlandite (wt.%) | Chemically bound water (wt.%) | Calcite (wt.%) |
|---|---|---|---|
| CEM I 52.5 N (No SP) | 9.42 | 3.40 | 2.25 |
| Batch 1 (SP 0.68%) | 6.09 | 3.82 | 1.94 |
| Batch 2 (SP 0.44%) | 6.76 | 3.23 | 2.57 |
| Micro-silica slurry (SP 0.24%) | 6.23 | 3.74 | 1.76 |

The results obtained by TGA/DTG were confirmed by XRD. A closer inspection of the XRD patterns (Fig. 17b) shows qualitatively the decreased intensities of the alite, belite, aluminate and ferrite phases in mortars with silica sludge (batches 1–2) and micro-silica compared to the reference sample, which is evident for higher hydration degrees. The main phases identified were quartz, calcite and portlandite. The hydrated phases identified were ettringite and in minor extent calcium monosulfoaluminate and monocarboaluminate. Other phases could not be identified in the XRD analysis as many peaks overlapped or are poorly crystalline. The TG/DTG and XRD results are consistent to the thermodynamically modeled expected phases for the complete hydration of Portland cement blended with $SiO_2$ [6,64]. For a concentration of 3 to 5% of $SiO_2$ (equivalent added with a 7% cement replacement by the different sludges) the expected phases are ettringite, portlandite, monocarboaluminate, hydrotalcite, calcite, aluminum hydroxide and jennite-like C–(A-)S–H gel.

### 3.5.3. Permeable (water accessible) porosity

The results of the measurements of the permeable or total porosity of the mortars are presented in Fig. 18. The results are surprisingly showing that the reference mortar has comparable porosity (19.1%) as the mortars containing silica sludge of batches 1–2 (19.4 and 19.5%, respectively). On the contrary, the mortar with micro-silica has the lowest total porosity (17.5%). The porosity and the tortuosity of the pores in the hardened cement paste are normally reduced when pozzolanic materials are added, and this influences many properties such as the compressive and splitting tensile strength [65]. Nevertheless, Yogendran and Langan [66] stated that for the addition of micro-silica the total pore volume is not necessarily changed, but larger pores appear to be subdivided into smaller pores. Apparently, the same behavior was found for the mortars containing silica sludge. In addition, it has been stated [6] that the partial replacement of cement with SCM leads to a decrease in the total volume of formed hydration phases. This means

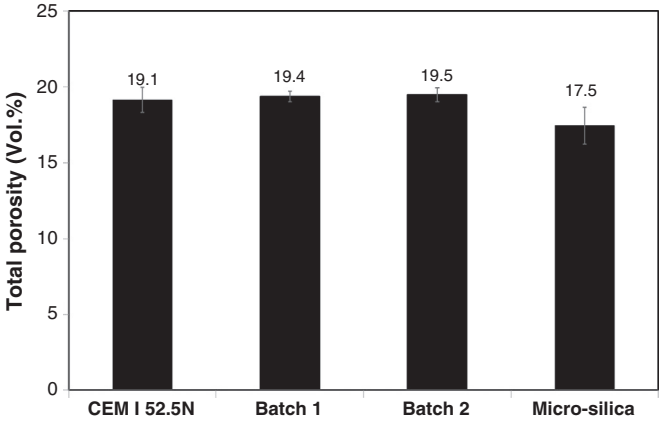


**Fig. 18.** Water permeable or accessible porosity at 28 days of the tested mortars.

that blended pastes have higher total porosities than 100% OPC pastes. This can be the reason of the high porosity values found. Another factor of influence is related to the different air content of the mortars. Some researchers [32] state that the vacuum-saturation technique is also able to take air voids into account. This means that the porosity values shown in Fig. 18 consider also the differences in the air content of the mixes (the lower the air content the lower the permeable porosity). This is in line with the lowest value of total porosity found for the micro-silica mortar which poses as well the lowest air void content (4%) and with the general microstructure observed by SEM analysis as described in Section 3.5.1. Even though the highest total porosity was measured for the silica sludge mortar a refined pore structure would be expected.

*3.5.4. Rapid Chloride Migration (RCM) test and conductivity test*

Fig. 19a shows the average values of the conductivity measured on hardened cylindrical reference mortars and the mortar with silica sludge of batches 1–2 and micro-silica. It is clearly demonstrated that the conductivity of the mortar is reduced by the silica sludge of batch 1 (−45%) and by the micro-silica (−79%) compared to the reference samples. Meanwhile, the mortar with the silica sludge of batch 2 presented a slightly lower conductivity than the reference sample (−3.5%). This behavior is an indication of the ability of the water saturated pore structure of the hydrated mortar to transport electrical charge. Different authors [67–69] established that the conductivity is directly related to the porosity, the pore structure (tortuosity, connectivity and conductivity) and to the pH of the pore solution (the pH in presence of amorphous silica is decreased, as was established in [34]).

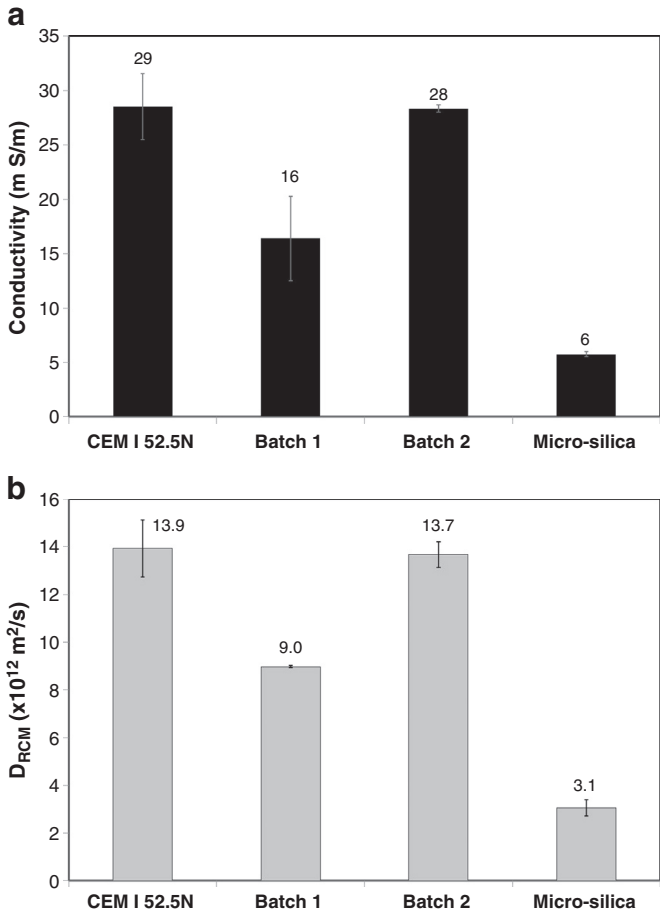


**Fig. 19.** 28 day results of the tested mortars, a) conductivity, b) chloride migration coefficient ($D_{RCM}$).

In general, higher porosity means higher conductivity due to the presence of more volumetric fractions of interconnected pores. The lower conductivity values shown by the mortars with high amount of nano-silica (batch 1 and micro-silica) are the result of the pore structure refinement (less connected pores) due to the progressive pozzolanic reaction and higher hydration degree (confirmed by TG/DTG and the microstructural analysis). Apparently, the lower concentration of $SiO_2$ (40.7%) and the highest concentration of $CaCO_3$ in batch 2 produced similar conductivity values compared to the reference sample. This behavior is consistent with the low hydration degree presented in this mortar (lower chemically bound water content). These results demonstrate that the replacement of cement by the silica sludge does not have adverse effects on the pore structures. On the contrary, similar or lower conductivities are obtained due to a refined pore structure. Thus, the improvement of the pore structure of concrete depends on the equivalent $SiO_2$ content of the silica sludge.

The Rapid Chloride Migration test (performed according to NT Build 492 [33]) is a commonly used accelerated technique for determining the chloride transport rate in concrete. The output of the test (the so-called chloride migration coefficient $D_{RCM}$) is employed in service-life design models for concrete elements and structures exposed to chlorides. This technique was employed in the standard mortar to assess the possible effect of the chloride content of the silica sludges on the durability of the hardened mortars. In this context, Fig. 19b presents the average values of the calculated chloride migration coefficient ($D_{RCM}$) of each mortar studied. Like the conductivity test results, the migration coefficients are much lower for the mixes containing high amounts of silica. The mortar with micro-silica shows again the best performance. The explanation for this behavior is the same as previously discussed for the conductivity test results. A finer porosity, greater tortuosity and more precipitated C–S–H gel reduce the ingress speed of chlorides into the mortars. In spite of the high chloride concentration of the silica sludge of batch 2 (1.9%), the $D_{RCM}$ coefficient of the mortar was slightly improved. This means that at replacement level as used in the present study (7% bwoc) no adverse effects on the durability of the hardened cement paste would be expected. Extra durability assessment should be performed for further replacement levels. On the contrary, if batch 1 is used to replace cement an extended durability would be expected.

## 4. Conclusions

In the present work, the physical and chemical characteristics of several photovoltaic's silica-rich sludges samples were determined and studied. The effect on the compressive strength of mortars due to the addition of stable slurries formulated of silica sludge was discussed. In addition, several assessment tests were conducted to investigate the potential use of photovoltaic's silica-rich waste sludge as supplementary cementitious material for concrete. A series of tests were carried out on mortars with 7% bwoc replacement level to compare the performance of the silica-rich sludge with those of micro-silica. Based on test results several conclusions can be drawn:

1. The silica sludge samples studied are composed of highly agglomerated nanoparticles and micro-sized waste particles. Their chemical analyses reveal a high content of amorphous $SiO_2$ and $CaCO_3$ with some impurities related to the additives used to prepare the original polishing slurries.
2. The dispersability study using a high-energy shear mixer demonstrated that it is possible to disperse the agglomerated particles of the original filter cake to nano-size. The resulting slurries are stable slurries and easy to prepare for the application in concrete.
3. The mechanical properties (flexural and compressive strength) of mortars with 7% bwoc of silica sludge are similar, and in some cases slightly higher, to the reference mortar. Therefore, the silica sludge of

batches 2 and 3 can be classified as a pozzolanic material having an activity index higher than 100.

4. The detail characterization of the hydrated system with photovoltaic's silica-rich waste demonstrated that the replacement of cement with this material influenced the amount and kind of formed hydration phases and thus the volume, the porosity and finally the durability of the tested mortars. At the level of substitution used in the present study, major changes are in the amount of chemically bound water (C–S–H gel formed), the consumption of portlandite, conductivity and chloride migration. At early age, filler and nucleating effects produced an increased reaction of the clinker phases; except for the silica sludge of batch 1 that had a retarding effect due to its content of water-soluble $P_2O_5$. In addition, it was found that the hydration of the aluminate phases is affected depending on the $CaCO_3$ and $SiO_2$ content of the studied sludge samples.

Even though positive results were obtained, further research is needed to study if this type of waste material can be supplied with a stable chemical composition. In addition, it is important to study the long-term effects on the concrete durability due to the high substitution levels which are due to the chloride content that was found in the sludge. The results demonstrate that the photovoltaic's silica-rich waste silica should be used as a potential SCM to partly replace cement in concrete, thereby decreasing the $CO_2$ footprint of concrete and the environmental impact associated with landfill of wastes.

## Acknowledgments

This research was carried out under the Project Number M81.1.09338 in the framework of the Research Program of the Materials innovation institute (www.m2i.nl) and The European Community's Seventh Framework Program, ProMine: Nano-particle products from new mineral resources in Europe, FP7-NMP-2008-LARGE-2 under Grant agreement 228559. The authors also wish to express their gratitude to P. Spiesz for his collaboration and following sponsors of the Building Materials Research Group at TU Eindhoven: Rijkswaterstaat Centre for Infrastructure, Graniet-Import Benelux, Kijlstra Betonmortel, Struyk Verwo, Attero, ENCI, Provincie Overijssel, Rijkswaterstaat Directie Zeeland, A&G Maasvlakte, BTE, Alvon Bouwsystemen, V.d. Bosch Beton, Selor, Twee "R" Recycling, GMB, Schenk Concrete Consultancy, Intron, Geochem Research, Icopal, BN International, APP All Remove, Consensor, Eltomation, Knauf Gips, Hess ACC Systems, Kronos and Joma International (chronological order of joining).

## References

[1] www.pvmarketresearch.com (consulted Dec. 2012).
[2] L.J. Fernandez, R. Ferrer, D.F. Aponte, P. Fernandez, Recycling silicon solar cell waste in cement-based systems, Sol. Energy Mater. Sol. Cells 95 (2011) 1701–1706.
[3] T.Y. Wang, Y.C. Lin, C.Y. Tai, R. Sivakumar, D.K. Rai, C.W. Lan, A novel approach for recycling of kerf loss silicon from cutting slurry waste for solar cell applications, J. Cryst. Growth 310 (2008) 3403–3406.
[4] M.S. King, H.C. Jung, H.S. Hong, G.S. Kim, H.S. Chung, A study of hot consolidation properties for recycled silicon powder, Curr. Appl. Phys. 11 (1) (2011) S54–S58.
[5] L. Fernandez-Carrasco, R. Ferrer, D.F. Aponte, S. Martinez-Ramirez, Stabilization of photovoltaic panels cell wastes in building material matrices, 1st Spanish National Conference on Advances in Materials Recycling and Eco-Energy, Madrid, 12–13 November, 2009, pp. 189–192.
[6] B. Lothenbach, K. Scrivener, R.D. Hooton, Supplementary cementitious materials, Cem. Concr. Res. 41 (2011) 1244–1256.
[7] A. Dunster, Silica fume in concrete, Information Paper No. IP 5/09, IHS BRE Press, Garston, U.K, 2009.
[8] G. Quercia, H.J.H. Brouwers, Application of nano-silica (nS) in concrete mixtures, in: Gregor Fisher, Mette Geiker, Ole Hededal, Lisbeth Ottosen, Henrik Stang (Eds.), 8th FIB International Ph.D. Symposium in Civil Engineering, Lyngby, Denmark: DTU Byg, 2010, pp. 431–436.
[9] G.J.M. Phylipsen, E.A. Alsema, Environmental life-cycle assessment of multicrystalline silicon solar cell modules, NOVEM Report 95057, Department of Science, Technology and Society, Utrecht University, September 2005, pp. 1–65.
[10] Y. Yamamoto, T. Yamada, T. Satou, M. Ishizuka, T. Kinoshita, N. Yasunaga, Development of polishing technique for silicon wafer, Advanced Materials and Optoelectronics, 3rd Technical report, Sumitomo Osaka Cement Co. Ltd., 2002, pp. 4–9.
[11] J. Min Kim, Y. Kwan Kim, Two possible ways of lowering the production cost of crystalline silicon wafers for solar cells, J. Ceram. Process. Res. 5 (3) (2004) 227–231.
[12] Y. Morioka, M. Kinoshita, Sh. Haba, An approach to slurry characterization for CMP, Nitta Haas Research Paper, PacRim-CMP, 2004, pp. 153–155.
[13] T.C. Lee, F.J. Liu, Recovery of hazardous semiconductor-industry sludge as a useful resource, J. Hazard. Mater. 168 (2009) 359–365.
[14] T.C. Lee, Recycling of municipal incinerator fly–ash slag and semiconductor waste sludge as admixtures in cement mortar, Constr. Build. Mater. 23 (2009) 3305–3331.
[15] T.C. Lee, K.L. Lin, X.W. Su, K.K. Lin, Recycling CMP sludge as resources in concrete, Constr. Build. Mater. 30 (2012) 243–251.
[16] C.J. Chang, L. Tseng, T.S. Lin, W.J. Wang, T.C. Lee, Recycling of modified MSWI ash–mix slag and CMP sludge as a cement substitute and its optimal composition, Indian J. Eng. Mater. Sci. 19 (February 2012) 31–40.
[17] British Cement Association, Emissions factor for cement provided by the British Cement Association. Available at www.bca.org.uk. June 2006.
[18] CEN EN 196-1, Methods of Testing Cement Part 1: Determination of Strength, European Commission for Standardization, 2005. 1–36.
[19] Activation Laboratories Ltd., Certificate of Analysis, Number A12-03763, A12-06724, June–April 2011. 1–6 (Canada).
[20] S. Brunauer, P.H. Emmett, E. Teller, Adsorption of gases in multimolecular layers, J. Am. Chem. Soc. 60 (1938) 309–319.
[21] DIN ISO 9277, Determination of the Specific Surface Area of Solids by Gas Adsorption Using the BET Method, German Institute of Normalization, 1995. 1–19.
[22] G. Thiele, M. Poston, R. Brown, A Case Study in Sizing Nanoparticles, Micromeritics Analytical Services, 2010. 1 (available at www.micromiretics.com).
[23] ISO 13320-1, Particle Size Analysis — Laser Diffraction Methods — Part 1: General Principles, International Organization for Standardization, CH-1211 Genève 20, Switzerland, 1999. 1–42.
[24] ISO 13321, Particle Size Analysis — Photon Correlation Spectroscopy, International Organization for Standardization, CH-1211 Genève 20, Switzerland, 2006. 1–108.
[25] Ltd Malvern Instruments, "Zeta Sizer Nano-User Manual — Zeta potential theory", MAN0317 Issue 5.0, August 2009. 265–275 (U.K.).
[26] L. Wadsö, Applications of an eight-channel isothermal conduction calorimeter for cement hydration studies, Cem. Int. (5) (2005) 94–101.
[27] J. Bensted, Some applications of conduction calorimetry, Adv. Cem. Res. 1 (1987) 35–44.
[28] J. Bensted, Chemical aspects of normal setting of Portland cement, in: J.F. Young (Ed.), Characterization and Performance Prediction of Cement and Concrete, United Engineering Trustees Inc., Washington, D.C., USA, 1983, pp. 69–86.
[29] H. Justnes, T. Ostnor, Pozzolanic, amorphous silica produced from the mineral Olivine, in: V.M. Malhotra (Ed.), Proceedings of the 7th CANMET/ACI International Conference on Fly Ash, Silica Fume, Slag, and Natural Pozzolans in Concrete vol. II, vol. 199, American Concrete Institute -ACI Special Publication, Chennai, India, July 22–27 2001, pp. 769–781.
[30] N. De Belie, J. Kratky, S. van Vlierberghe, Influence of pozzolans and slag on the microstructure of partially carbonated cement paste by means of water vapour and nitrogen sorption experiments and BET calculations, Cem. Concr. Res. 40 (2010) 1723–1733.
[31] ASTM C1202, Standard Test Method for Electrical Indication of Concrete's Ability to Resist Chloride Ion Penetration, Annual Book of ASTM Standards, vol. 04.02, American Society for Testing and Materials, Philadelphia, July 2005, pp. 1–6.
[32] Md Safiuddin, N. Hearn, Comparison of ASTM saturation techniques for measuring the permeable porosity of concrete, Cem. Concr. Res. 35 (2005) 1008–1013.
[33] Nordtest method NT Build 492, Concrete, Mortar and Cement-Based Repair Materials: Chloride Migration Coefficient from Non-Steady-State Migration Experiments, 1999. 1–8 (Finland).
[34] P. Spiesz, M.M. Ballari, H.J.H. Brouwers, RCM: a new model accounting for the nonlinear chloride binding isotherm and the non-equilibrium conditions between the free- and bound-chloride concentrations, Constr. Build. Mater. 27 (2012) 293–304.
[35] R.B. Polder, Test methods for onsite measurement of resistivity of concrete a RILEM TC-154 technical recommendation, Constr. Build. Mater. 15 (2001) 125–1301.
[36] H.L. Sheng, R.Y. Chung, Chemical and physical treatments of chemical mechanical polishing wastewater from semiconductor fabrication, J. Hazard. Mater. B108 (2004) 103–109.
[37] W. Dena, Ch. Huang, Electrocoagulation for removal of silica nano-particles from chemical–mechanical-planarization wastewater, Colloids Surf., A Physicochem. Eng. Asp. 254 (2005) 81–89.
[38] P.A. Budiman, Treatment of Chemical Mechanical Polishing Waste Water of Semiconductor Manufacturer. (Thesis for Master degree) National Taiwan University of Science and Technology, Taiwan, April 2006. 1–96.
[39] NEN EN 13263-1 A1, Silica Fume for Concrete — Part 1: Definitions, Requirements and Conformity Criteria, Netherlands Standardization Institute, 2005. 1–29.
[40] CUR, Vliegas als vulstof in beton, Civieltechnisch Centrum Uitvoering Research en Regelgeving, Gouda, 1992.
[41] DIN EN 196-2, Methods of Testing Cement Part 2: Chemical Analysis of Cement; German Version EN 196-2:2005, German Institute of Normalization, 2005. 1–52.
[42] International Union of Pure and Applied Chemistry (IUPAC), Reporting data for gas/solid systems with special reference to the determination of surface area and porosity, Pure Appl. Chem. 57 (4) (1985) 603–619.
[43] ECETOC JACC REPORT No. 51, Synthetic Amorphous Silica (CAS No. 7631-86-9), European Centre for Ecotoxicology and Toxicology of Chemicals, Brussels, September 2006. 1–231.
[44] A.W. Pacek, P. Ding, A.T. Utomo, Effect of energy density, pH and temperature on de-aggregation in nano-particles/water suspensions in high shear mixer, Powder Technol. 173 (2007) 203–210.

[45] N.G. Özcan-Taskin, G. Padron, Effect of particle type on the mechanisms of breakup of nanoscale particle clusters, 13th European Conference on Mixing, London, April 14–17 2009, pp. 1–8.
[46] P. Ding, M.G. Orwa, A.W. Pacek, De-agglomeration of hydrophobic and hydrophilic silica nano-powders in high shear mixer, Powder Technol. 195 (2009) 121–226.
[47] G. Padron, W.P. Eagles, N.G. Özcan-Taskin, G. McLeod, Effect of particle properties on break up of nanoparticle clusters using an in-line rotor–stator, J. Dispers. Sci. Technol. 29 (2008) 580–586.
[48] M. Goa, E. Frossberg, Prediction of product size distribution for a stirred ball mill, Powder Technol. 84 (1995) 101–106.
[49] K. Kendall, C. Staiton, Adhesion and aggregation of fine particles, Powder Technol. 121 (2001) 223–229.
[50] S. Mende, F. Stenger, W. Peukert, J. Schweder, Mechanical production and stabilization of submicron particles in stirred media, Powder Technol. 132 (2003) 64–73.
[51] R. Wengeler, H. Nirschl, Turbulent hydrodynamic stress induced dispersion and fragmentation of nanoscale agglomerates, J. Colloid Interface Sci. 306 (2007) 162–273.
[52] K. Ralph, Iler, The Chemistry of Silica: Solubility, Polymerization, Colloid and Surface Properties, and Biochemistry, Wiley, New York, 1979.
[53] B. Lothenbach, G. Le Saout, M.B. Haha, R. Figi, E. Wieland, Hydration of a low-alkali CEMIII/B-$SiO_2$ cement (LAC), Cem. Concr. Res. 42 (2012) 410–423.
[54] P. Hou, Sh. Kawashima, D. King, D.J. Corr, J. Qian, P. Shah, Modification effects of colloidal nano-$SiO_2$ on cement hydration and its gel property, Compos. Part B 45 (1) (2013) 440–448.
[55] M.H. Zhang, J. Islam, S. Peethamparan, Use of nano-silica to increase early strength and reduce setting time of concretes with high volumes of slag, Cem. Concr. Compos. 34 (2012) 650–662.
[56] L. Nicoleau, The acceleration of cement hydration by seeding: influence of cement mineralogy, in: H.-B. Fischer, K.-A. Bode, C. Beuthan (Eds.), Proceedings of the 18th International Conference on Building Materials (IBAUSIL 2012), 12. Bis 15. September, Weimar, Germany, Bauhaus-University, Weimar, Germany, 2012, pp. 1–13.
[57] H.F.W. Taylor, Cement Chemistry, 2nd editions Thomas Telford Edition, 1997. 1–459.
[58] P.C. Hewlett, Lea's Chemistry of Cement and Concrete, 3th edition John Wiley & Son Inc., New York, 1988. 1–1053.
[59] K. van Breugel, Simulation of Hydration and Formation of Structure in Hardening Cement-Based Materials. (PhD. Thesis) Delft University of Technology, Delft, The Netherlands, 1991. 1–305.
[60] E.B. Nelson, D. Guillot, Cement additives and mechanism of action, chapter 3, Well Cementing, second editions, Schlumberger ltd., Sugar Land, Texas, U.S.A, 2006. 71–80.
[61] A.M. Neville, Properties of Concrete, 4th ed. Prentice Hall/Pearson, Harlow, U.K., 2000. 1–844.
[62] B.V. Enci, Betonpocket 2010, Heidelberg Cement Group, 's-Hertogenbosch, The Netherlands, 2009. 1–288 (in Dutch).
[63] V.S. Ramachandran, R.M. Paroli, J.J. Beaudoin, A.H. Delgado, Handbook of Thermal Analysis of Construction Materials, William Andrew Publishing, Norwich, New York, U.S.A., 2002. 1–680.
[64] B. Lothenbach, E. Wieland, A thermodynamic approach to the hydration of sulphate-resisting Portland cement, Waste Manage. 26 (2006) 706–719.
[65] E.J. Garboczi, Permeability, diffusivity, and microstructural parameters: a critical review, Cem. Concr. Res. 20 (1990) 591–601.
[66] V. Yogendran, B.W. Langan, Utilization of silica fume in high strength concrete, Proceedings of Utilization of High Strength Concrete, Stavanger, Tapir Publisher, Trondheim, Norway, 1987.
[67] D. Desmet, J. Hernandez, L. Willain, J. Vantomme, Porosity determination of selfcompacting concrete using forced saturation, Proceeding of the XIII International Conference on Cement Chemistry, Madrid, July 4–8 2011, pp. 1–7.
[68] C. Andrade, R. D' Andrea, J.C. Lopez, A. Cienfuegos-Jovellano, J.M. Alvarez, J.M. Millan, Use of electrical resistivity as complementary tool for controlling the concrete production, Proceeding of the XIII International Conference on Cement Chemistry, Madrid, July 4–8 2011, pp. 1–7.
[69] C. Andrade, O. Rio, A. Castillo, M. Castellote, R. D' Andrea, A NDT Performance method based on electrical resistivity for the specification of concrete durability, ECCOMAS Thematic Conference on Computational Methods in Tunnelling, Vienna, Austria, August 27–29 2007, pp. 1–9.
[70] M. Hunger, Chemical and Mineralogical Composition of CEM I 52.5 N Manufactured at ENCI B.V, Maastricht Facilities, The Netherlands, May 2013. (Personal communication).
[71] G. Hüsken, A Multifunctional Design Approach for Sustainable Concrete: With Application to Concrete Mass Products. (PhD. Thesis) Eindhoven University of Technology, No. 148, Eindhoven, The Netherlands, 2010. 109.